Journal Pre-proof

Are slump folds reliable indicators of downslope flow in recent mass transport deposits?

G.I. Alsop, R. Weinberger

PII: S0191-8141(19)30446-8

DOI: https://doi.org/10.1016/j.jsg.2020.104037

Reference: SG 104037

To appear in: *Journal of Structural Geology*

Received Date: 24 October 2019

Revised Date: 12 February 2020

Accepted Date: 4 March 2020

Please cite this article as: Alsop, G.I., Weinberger, R., Are slump folds reliable indicators of downslope flow in recent mass transport deposits?, *Journal of Structural Geology* (2020), doi: https://doi.org/10.1016/j.jsg.2020.104037.

G.I. Alsop – Fieldwork, conceptualization, writing

R. Weinberger - Fieldwork, conceptualization, writing

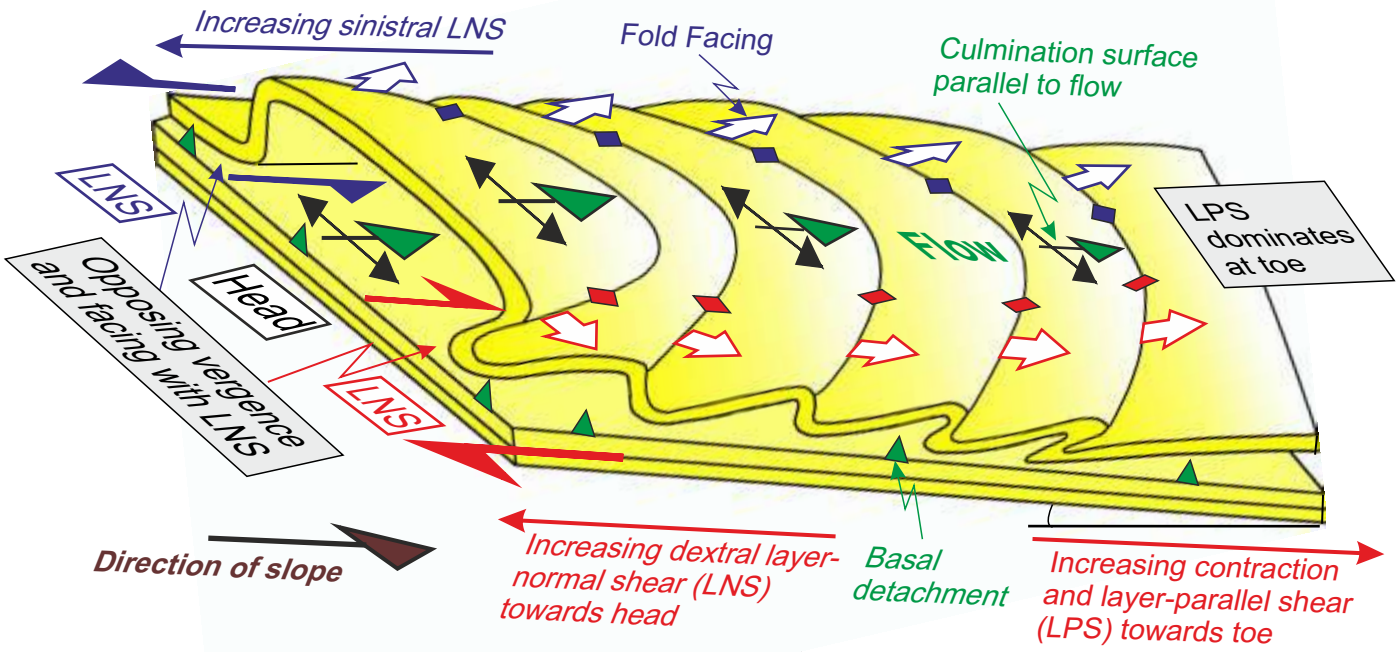

Are slump folds reliable indicators of downslope flow in recent mass transport deposits?

G.I. Alsop[1], R. Weinberger[2, 3]

1) Department of Geology and Geophysics, School of Geosciences,
University of Aberdeen, Aberdeen, UK. (e-mail: Ian.Alsop@abdn.ac.uk)
2) Geological survey of Israel, Jerusalem, Israel.
3) Department of Geological and Environmental Sciences, Ben Gurion University of the Negev, Beer Sheva, Israel.

Abstract

Despite the widespread use of slump folds as indicators of palaeoslope orientation, there is a lack of detailed analysis of variations in fold geometries and orientations down the length of individual slump profiles within mass transport deposits (MTDs). To address this gap in knowledge, we have systematically recorded more than 500 structural measurements of fold hinges and axial planes along a 25 m section through a mesoscopic slump profile. Our case study is performed in wet unconsolidated (late Holocene) sediments, which are only recently exposed due to falling water levels in the Dead Sea. In this situation, the modern slope is exposed and directly visible, slumping having occurred in the past few centuries. Fold hinges define broad arcs at high angles to flow in the downslope toe of the slump and progressively swing to become sub-parallel to flow in the upslope region. Greatest amounts of shortening (~35%) are recorded at the toe, suggesting that the swing in trends of fold hinges and axial planes is a consequence of differential layer-normal shear rather than downslope strain gradients. Significant variations of >90° occur in the orientation and vergence of slump folds on either side of a 10 m wide gully, which cuts the slump sheet. In some instances, folds have nucleated around longer (>10 cm) wooden sticks that were incorporated into the slump, whereas shorter wooden fragments align parallel to the flow direction. The differences in orientations of wooden sticks and wooden fragments are consistent with differential layer-normal shear on each side of a flow cell. Evaporite concretions grew within the sediments during slumping and influenced the geometry and kinematics of slump folds, suggesting that slope failure may have been a slow 'creep' event generated by slope instability, rather than a result of catastrophic failure associated with large earthquakes. Our work illustrates the problems associated with using partial datasets, where classical structural analysis of transects <10 m apart would incorrectly suggest slump directions opposed to one another by 90°. This study thereby highlights the extreme variability within a downslope profile of a single slump. It may therefore help explain discrepancies in regional datasets where slumps, sporadically sampled at different stratigraphic levels, may provide apparently diverse flow directions.

Keywords. MTD; slump; fold; palaeoslope; Dead Sea; Ze'elim Formation

1. Introduction

Slump folds develop where unlithified sediments move downslope under the influence of gravity. They form part of mass transport deposits (MTDs) that develop across a range of scales in subaqueous settings (e.g. Gibert et al., 2005; Morley et al., 2011; Scarselli et al., 2016; Reis et al., 2016; Korneva et al., 2016; Basilone 2017). Slump folds have been identified in rocks since the end of the 19th century (McGee 1891, quoted in Woodcock, 1979, p.83; for a historical review see Maltman 1994) and are one of the most widely used indicators of palaeoslope orientations and hence palaeogeography (e.g. Woodcock, 1976a, b; Strachan and Alsop, 2006). Although some uncertainties may occur in lithified rocks that have undergone hard rock deformation (HRD) as to which folds may be tectonic in origin and which relate to soft sediment deformation (SSD) (Waldron and Gagnon, 2011), slump folds are typically considered robust indicators of downslope flow of unlithified sediments (see Alsop et al.,

2019 for a review). Despite the widespread application of slump folds to estimate the attitude of palaeoslopes, there has been little analysis of fold patterns in modern basinal settings to measure the variation of slump fold orientations and geometries and hence test their validity in slope analysis.

Recent advances and improvements in seismic resolution from large scale MTDs have enabled the broad geometric framework of modern slope failures to be deduced (e.g. Frey Martinez et al., 2005; Jolly et al., 2016; Scarselli et al. 2016; Steventon et al. 2019). Failure is thought to develop along an underlying basal detachment, above which extension is generally considered to form fault scarps in the upslope head, while the downslope toe is marked by contraction linked with folding and thrusting that is associated with layer-parallel shear (LPS) along the basal detachment (e.g. Farrell, 1984; Farrell and Eaton, 1987; Garcia-Tortosa et al., 2011; Alsop et al., 2020a, b). The toes of MTDs may be broadly divided into 'frontally-confined', where the MTD is constrained and buttressed by unmoved downslope sediments, and 'frontally-emergent' where the MTD ramps up and over the downslope sediments to flow freely on the seafloor (Frey-Martinez et al., 2006). The flanks of MTDs are marked by zones of downslope-trending strike slip or differential layer-normal shear (LNS) that enable flow cells of sediment to move at different rates downslope, and thereby divide the toe of an MTD into a series of individual sediment 'lobes' (e.g. Debacker et al., 2009; Sharman et al., 2015; Alsop et al., 2020c).

Despite these recent developments stemming from bathymetric mapping of the sea floor combined with seismic analysis of gravity-driven fold and thrust belts that form large scale MTDs (e.g. Corredor et al., 2005; Zalan, 2005; Bull et al., 2009; de Vera et al. 2010; Armandita et al., 2015; Totake et al., 2018) , the details of folding are typically below the limits of seismic resolution. In addition, sediment cores may provide biased sampling that does not encompass a wide enough area to interpret larger folds or complex fold detail (see discussion in Lu et al., 2017). Analysis of folding associated with SSD in outcrops is typically performed on older rocks (e.g. Woodcock 1976a, b, 1979, Strachan and Alsop 2006; Van der Merwe et al., 2011) where the palaeogeographic constraints are more limited and the use of slump folds to determine flow and hence palaeoslope orientations may become more problematic.

Rapid fall in water levels of 1 m per year in the Dead Sea have not only revealed recent unconsolidated MTDs in this seismically active basin, but have also led to increased downcutting of wadi outlets to reach the new 'base level'. The combination of slope instabilities, falling water levels, and increased gully incision to provide profiles and sections through the slumps means that this area is ideally suited to a detailed analysis of slump fold patterns formed at the toe of an MTD. In particular, we address a number of general questions that are applicable across a range of scales and basin settings:

i) What triggers slumping and does it reflect creep or catastrophic slope failure?

ii) How reliable are different methods of determining palaeoslope?

iii) What kinematic models best explain variable fold geometries in MTDs?

iv) How do layer-parallel and layer-normal shear components vary along a slump profile?

We first outline four general models that may be used to explain variable slump fold patterns around the toes of MTDs, before discussing the Dead Sea case study in greater detail.

2. Models of folding and flow

In order to use slump folds as estimators of palaeoslope (Woodcock, 1979), we must understand the kinematics of their development and how they relate to the slope in question. Many of the models that have been developed to understand fold kinematics in metamorphic terranes and thrust sheets may equally be applied to gravity-driven fold and thrust systems that move downslope to create MTDs (e.g. Coward and Potts, 1983; Alsop and Holdsworth, 1993; Xypolias and Alsop, 2014). Variation in flow direction and flow velocity around flow cells or 'lobes' may result in a range of four fold scenarios and kinematic models within MTDs (Fig. 1).

2.1.1. Variable flow direction and constant flow velocity

A simple explanation for variable fold hinge trends and axial planar orientations in MTDs is to invoke variable flow directions marked by relatively constant velocities that radiate away from the centre of a slump (Fig. 1a). Such 'radial spreading' results in a fanning of fold hinge and axial plane orientations and is typically developed where the toes of slumps and MTDs have become frontally-emergent (Frey-Martinez et al., 2006) leading to unconstrained flow over the downslope sediment. Fold hinges display an arc of orientations and typically verge away from the flow lobe, while axial planes generally dip towards the centre of the lobe. Such radial flow has been previously invoked to explain variable fold orientations around the toes of slumps (see Strachan and Alsop, 2006). Radial flow may result in circumferential extension along the leading outer arc marked by stretching parallel to fold hinges, whilst Fossen (2016, p. 388, fig. 18.12) also notes a "divergent displacement field" around the toe of slumps.

2.1.2. Variable flow direction and variable flow velocity

A modification of the above model involves variable fold hinge trends and axial planar orientations created by variable flow directions in association with variable flow velocities (Fig. 1b). In this scenario, variable rates of radial spreading are accommodated by differential shear around a central 'surging' flow lobe. Zones of both sinistral and dextral layer-normal shear (LNS) may be created on each side of the flow lobe as in classical models of layer-normal shear (see Coward and Potts, 1983; Alsop and Holdsworth, 1993; 2007). However, an important distinction from such models is that the flow direction is not constant and is directed away from the centre of the lobe.

2.1.3. Constant flow direction and constant flow velocity

Layer-parallel shear (LPS) develops where flow maintains a relatively constant direction and along-strike velocity (Alsop and Holdsworth, 1993 2007). In this situation, downslope-verging fold hinges and associated axial planes may define broad arcs in orientations due to fold rotation into the flow direction during progressive shear (Fig. 1c). Fold hinges that are in initially anticlockwise of flow undergo clockwise rotation, while initially clockwise-trending hinges are subject to anticlockwise rotation towards the flow direction (Fig. 1c). Increasing rotation of fold hinges towards the flow direction results in a decrease in the apical angle between opposite ends of a curvilinear fold, as defined by Alsop and Holdsworth (2012, their table 1) (Fig. 1c). Such patterns are widely observed in metamorphic terranes and MTDs where a significant component of LPS is developed (e.g. Alsop and

Holdsworth, 2007). Rotation of fold hinges into the flow direction requires significant strain that leads to tightening of fold hinges and flattening of axial planes into the shear plane and may ultimately result in highly-curvilinear sheath fold geometries (Alsop and Holdsworth, 2007).

2.1.4. Constant flow direction and variable flow velocity

It has long been recognised in metamorphic terranes that constant flow directions associated with variable velocities along strike create an arc of fold orientations associated with flow perturbations and layer-normal shear (LNS) (e.g. Coward and Potts, 1983; Alsop and Holdsworth 1993). Such models apply equally to flow within MTDs, where differential sinistral shear generates fold hinges with a clockwise obliquity to flow, whereas differential dextral shear creates anticlockwise-trending hinges (Alsop and Holdsworth 2007; Alsop and Marco, 2014; de lima Rodrigues et al. 2020) (Fig. 1d). An important distinction between this LNS model, and that described above involving intense LPS (Fig. 1c), is that folds generated oblique (<45°) or sub-parallel to flow have not undergone significant rotation and may not be markedly tightened and may not therefore show axial planes rotated into the shear plane.

3. Geological setting

The Dead Sea Basin (DSB) is a pull-apart structure developed between two left-stepping strands of the Dead Sea Fault (DSF) system (Fig. 2a, b; Garfunkel, 1981; Quennell, 1958). The basin is bounded by a series of oblique-normal faults that juxtapose Cretaceous carbonate rocks against Quaternary alluvial and lacustrine sediments along the basin's western margin (Fig. 2b, c). The Dead Sea is a terminal lake, the youngest of a series of lakes that have occupied the basin since the Upper Miocene. Holocene and late Pleistocene fan-deltas are very common deposits along the western margins of the Dead Sea (e.g., Sneh, 1979; Bowman, 1974; Manspeizer, 1985). The Ze'elim Wadi is one of the largest wadis along the western margin of the Dead Sea, and its associated fan-delta is incised into the fluvial-lacustrine sequence of the late Pleistocene Lisan Formation (Begin et al., 1974). To the east and below the ca.- 400 m mean sea level (m.s.l.) contour, it is dominated by mudflats consisting of 20–40 m of alternating layers of detrital and chemical (mainly aragonite) laminae as well as clay, silt, sand, salt, and gravel of the Holocene Ze'elim Formation, with a ~10 ka salt layer at its base (Yechieli et al., 1993; Ken-Tor et al., 2001). The western margin of the basin displays a 4° to 6° slope, which steepens up to 20° along a shore-margin strip (Coianiz et al., 2019). This area was first exposed during the late 1970s in response to a drop in Dead Sea water level and is currently undergoing rapid gully incision (Avni et al., 2016).

The Ze'elim Formation records deformation (e.g. seismites, liquefaction) which are associated with earthquakes related to the DSF (Enzel et al., 2000; Ken-Tor et al., 2001; Kagan et al., 2011). It is currently exposed around the margins of the Dead Sea (Fig. 2b) and has also been recovered from drill cores taken from nearer the depocentre of the basin (Lu et al., 2017; Kagan et al., 2018). Here we focus on soft-sediment deformation and MTDs located in the northernmost part of the fan in the Ze'elim 3 gully (e.g. Kagan et al., 2011) (Fig. 2c, d). Due to the ongoing fall in water levels in the Dead Sea of ~1 m per year, the Ze'elim 3 gully continues to incise deeper into the underlying Ze'elim Formation, thereby exposing recent MTDs in the walls of the gullies (Fig. 2e-g). As the studied slump profile sits directly beneath modern gravels that form the Ze'elim fan, that emanates from the Ze'elim wadi, the section is believed to be the very youngest part of the Ze'elim Formation (Fig. 2e-g, k).

Structural data for this study were collected in March 2014 close to where the Ze'elim 3 gully enters the Dead Sea, before wash-out and erosion of the canyon walls during a flash flood event in

March 2015 (Fig. 2c-k). Continued incision of the gully was examined subsequently in 2017 and 2019 but has not revealed any further structural features related to the case study slump, which is traced for 25 m in the gully (Figs 2j, 3a). The Ze'elim 3 gully incises across this slump, the NW side of the gully trending 045° while the SE wall trends 064°. These divergent walls result in an increase in the width of the gully from 5 m at the head of the slump to 10.5 m at the downslope toe (as of March 2014). In the ideal situation, it has long been recognised (e.g. Jones, 1939) that the strike of bedding is parallel to the trend of the slope while the dip direction is directly down the slope meaning that bedding forms parallel to the slope. Measured bedding adjacent to the case study slump displays a mean orientation of 132/06NE, suggesting that the depositional slope is towards 042°. The toe of the slump as exposed on both the NW and SE sides of the gully. A line joining these fixed points trends 130°, indicating that the termination of the slump was approximately parallel to the strike of the slope.

4. Structural elements

More than 500 structural measurements of fold hinges and axial planes were taken from 25 m sections forming the SE and NW sides of the gully incised along the slump profile, making this one of the most intensively studied slumps ever recorded (Figs 2d-k, 3a, 4a-k, 5a-j). In addition, fold facing, which is defined as the direction normal to the fold hinge, and along the axial plane, in which younger rocks are encountered (Holdsworth, 1988) was also calculated for each fold based on graded bedding in the sequence (Figs 3a, e-g, 4a-k, 5a-j). For the purposes of statistical analysis, an approximately equal number of folds were sampled from the SE side (N=131) and NW side (N=130) of the gully (Fig. 3a-d). The toe of the slump is marked by deformation dying out downslope into undeformed beds within 1 m of the lowermost thrust (Figs 4a, 5a, 6a, b). The upslope head is marked by attenuated beds and evaporite concretions, although no clear extensional faults are developed in contrast to classical models of slump folding and MTDs (e.g. Farrell, 1984; Bull et al., 2009) (Figs 4i-k, 5h-j). Beds above and below the slumped sequence dip at 5°NE (042°) which represents the downslope direction controlling gravity-driven slump movement.

4a) SE Gully

A complete photographic profile down the SE side of the gully, together with highlighted marker beds and associated stereoplots for each 2.5 m section is presented in Fig. 4a-k, while Table 1 provides a summary of mean fold hinge and axial planar orientations. Sub-horizontal to gently-plunging fold hinges exposed on the SE side of the gully trend N-S to NE-SW, and consistently verge towards the east or SE (Fig. 3a, b, e). Fold hinges are universally upward-facing towards the east and SE, while fold axial planes dip gently to moderately towards the west (Figs 3a, b, 4a-k). Analysis of fold hinges and axial planes for each 5 m segment of the SE gully shows that fold hinges display clustered distributions, while axial planes also show reasonably constant strikes, although amounts of dip are more variable, leading to trails of axial-planar poles on stereoplots (Figs 3e, 4a-k). Taken in isolation, structural measurements from the SE gully form a coherent data set associated with east or SE-verging folds.

4b) NW Gully

A complete photographic profile down the NW side of the gully, showing highlighted marker beds and associated stereoplots for each 2.5 m section, is presented in Fig. 5a-j, while mean fold data are displayed in Table 1. Sub-horizontal to gently-plunging fold hinges exposed on the NW side of the gully trend NW-SE to NE-SW, and consistently verge towards the NW or NE (Fig. 3a, c, f). Fold hinges are universally upward-facing towards the NW and NE, while fold axial planes dip gently to moderately towards the SW or SE (Figs 3a, c, f, 5a-j). Analysis of fold hinges and axial planes for each 5 m segment of the NW gully shows that fold hinges display clustered distributions, while axial planes also show reasonably constant strikes, although measurements of dip are more variable leading to trails of axial-planar poles on stereoplots (Figs 3f, 5a-j). Taken in isolation, structural measurements from the NW gully form a coherent data set associated with NW or NE-verging folds.

4c) Combined SE and NW Gully

Collective examination of slump fold measurements from both the SE and NW sides of the gully allows us to compare and combine data sets (Fig. 3a, d, g). The normal to the mean SE and NE verging fold hinges from the SE and NW sides of the gully trends towards 051° (Fig. 3a, g) and is relatively constant along the slump profile. Similarly, the bisector of the fold facing directions is also relatively constant towards 052° along the length of the slump profile (Fig. 3a, g). The calculated intersection of mean axial planes from SE and NE verging folds displays a little more variation along the profile from 030° to 073°, but on average is towards 044° (Fig. 3a, g).

5. Structural analysis along the slump profile

5.1. Thickness variation along the slump profile

The thickness of the slump sheet was measured at 1 m intervals up the SE and NW sides of the gully from the toe to the head (Fig. 7a). In addition, the amount of shortening recorded by folds and thrusts affecting a (yellow) marker layer shown in Figs 4a-k, 5a-j, 6a-f was also estimated. This estimate of shortening does not include any component of lateral compaction that may have affected the slump sheet (see Butler and Paton, 2010 and Alsop et al. 2017a, b) or subsequent modification of original buckle fold geometries, and as such is purely a general guide to shortening.

The thickness of the undeformed sequence at the toe of the slump varies between 8 cm and 13 cm on the SE and NW sides of the gully respectively, with the thickness of the deformed sequence increasing to ~20 cm at 5 m further upslope (Fig. 7a). Although the marker layer records no deformation at the defined toe (0 m), shortening rapidly increases (to ~35%) in the lowest 2.5 m. This lowermost segment of the slump profile is dominated by recumbent to upright folds with occasional low-angle thrusts which are highly effective at shortening, but do not necessarily create the maximum thickening in the slump profile (Figs 4a-c, 5a-c, b, 6a, b, 7a). From 2.5 to 15 m, the slump sheet displays further thickening to reach a maximum thickness of ~25 cm at 10 to 15 m (Fig. 7a). This central portion of the slump profile is dominated by upright folds together with box folds that display axial planes dipping in opposing directions approximately up and down slope (Figs 4c-g, 5c-g, 6c-f). Although this central section does not display the greatest amount of shortening, it does form the most thickened part of the slump profile due to the upright nature of the folds and box folds (Figs 6c-f, 7a). From 15 to 25 m, the slump profile displays a progressive reduction in thickness, that becomes most pronounced from 22 to 25 m where the thickness reduces from 17 to 20 cm to 7 to 10 cm at the head

(Fig. 7a). This upper section of the slump profile is marked by more sporadic upright to inclined folds and internal detachments within the slump that do not necessarily affect the yellow marker bed (Figs 4h-k, 5h-j). In summary, the slump section displays a 'bell-shaped' thickness profile with marked (2 to 3 times) thickening in the central segment away from the toe and head. Although the amount of shortening recorded by the yellow marker is estimated to reach a maximum (~35%) near the toe, the low angle attitude of folds and thrusts observed here does not markedly thicken the profile (Fig. 7a).

5.2. Fold hinge variation along the slump profile

Fold hinge trends measured from the SE side of the gully display a 34° clockwise swing in mean trend from 181° at the toe of the slump to 215° at the head of the slump, whereas hinge trends from the NW side display a 69° anticlockwise swing in mean trend from 114° at the toe of the slump to 045° at the head (Figs 3a, e, f, 7b). This variation in fold hinge orientation towards NE-SW trends is not linked to an increase in fold tightness (Figs 4a-k, 5a-j). If we compare fold hinge orientations with the direction of the slope (042°), then fold hinges from the SE side are orientated anticlockwise to the downslope direction (and display less variation) relative to fold hinges from the NW side which are clockwise of 042° (Figs 7c, 8a). Comparing fold hinge and axial plane orientations from each side of the gully and equivalent distances up the slump profile reveals that the greatest obliquities (>90°) are recorded at 0 to 5 m from the toe of the slump, and these reduce (<90°) at 5 to 15 m up the slump until obliquities of <45° are measured at the top (20 to 25 m) of the profile (Fig. 7d, Table 1). This corresponds to a general opening and increase of the statistical apical angle (see Fig. 1c) down the slump profile and towards the toe (Fig. 7d).

5.3. Fold axial planar variation along the slump profile

The dip direction of fold axial planes measured from the SE side of the gully display a 52° clockwise swing in mean trend from 262° at the toe of the slump to 314° at the head of the slump, whereas axial plane dip directions from the NW side display a 75° anticlockwise swing in mean trend from 208° at the toe of the slump to 133° at the head (Figs 3a, e, f, 7e, f). Some axial planes dip in opposing directions where they form 'box fold' geometries (e.g. Fig. 6d-f) and this is reflected in a smaller subset of data on Fig. 7e. As with fold hinges, the axial planes from the SE side display less variation when compared to the NW side (Figs 7e, f, 8b). Examination of axial-planar strike relative to the orientation of the slope (042°), reveals that the axial planes from the SE gully are consistently anticlockwise of the slope direction while those from the NW gully are clockwise (Figs 3a, e, f, 8b). Fold axial planes from the SE gully display a progressive clockwise swing in strike from the toe to the head of the slump, whereas axial planar strike from the NW gully shows a gradual anticlockwise swing from the toe to head of the slump (Figs 3a, e, f, 8b, Table 1). Although axial planes dip in opposing directions from the SE and NW sides of the gully, the angle between axial planar strikes from each side of the gully and equivalent distances up the slump profile displays a progressive reduction from 128° at the toe, to <90° at 5 to 15 m up the profile, to <45° at the head of the slump (Fig. 7d). For each fold, the trend of the fold hinge and the strike of the associated axial plane therefore vary in tandem up the profile, meaning that fold hinges are generally sub-horizontal and pitch at very low angles on their axial planes (Fig. 7g). As mean fold trend varies up the SE and NW side of the profile, the dip of the associated mean axial plane also changes, such that axial planes towards the lower end of the slump tend to have steeper dips, whereas axial planes towards the head display shallower dips (Fig. 7h). At

the very toe however, the axial planar dip actually decreases as structures become dominated by recumbent folds and thrusts (Figs 4a, b,5a, b, 6a, b,7h).

5.4. Fold Facing variation along the slump profile

Mean fold facing directions measured from the SE side of the gully display a 37° clockwise swing from 088° at the toe of the slump to 125° at the head of the slump, whereas hinge trends from the NW side display a 70° anticlockwise swing in mean trend from 025° at the toe of the slump to 315° at the head (Figs 3a, e, f, 4a-k, 5a-j, 8c). Fold facing direction is therefore consistently clockwise of the downslope direction SE of the gully, and anticlockwise on the NW side (Fig. 8c). The variation in facing direction reflects the previously described swing in fold hinge trend and axial planar orientation.

6. Evaporite concretions

Evaporite laminae and concretions that form mushroom shapes are created just offshore in the modern Dead Sea. During the Holocene, the hypersaline waters of the Dead Sea similarly allowed evaporite minerals (aragonite, gypsum) to precipitate in the form of laminae and concretions in the Ze'elim Formation. Metre-scale concretions that formed in the studied section (Figs. 4k, 9a) were studied by XRD at the Geological Survey of Israel and are composed of gypsum with minor components of aragonite and Bassanite ($2CaSO_4 \cdot H_2O$). These concretions are exposed at the upper end (head) of the slumped sediments, particularly on the SE side of the gully (Figs 4k, 9a). The overlying beds are arched upwards over the top of the concretions, while lower beds are deflected downwards below the concretions (Fig. 9a-d). Concretions are too large to be 'washed in' with adjacent fine grained detritals, while the lack of significant disruption and breaking of laminae around them suggests they have not rolled downslope. The absence of significant overburden with which to load the slump means that differential compaction is not created around the evaporite concretions. We therefore suggest that the concretions grew *in-situ*, causing bending and attenuation of surrounding beds as they penetrated both upwards and downwards.

While downward-deflected bedding does not display any significant change in facies or thickness of layering, there are a variety of observations from the overlying beds that suggest concretions initially grew during sedimentation and had a bathymetric expression on the lake floor. Firstly, stratigraphic packages, including the studied slump horizon, thin over the crest of the evaporite concretions, suggesting that concretions directly affected sedimentation on the lake floor (Fig. 9a, b). Secondly, mud-rich detrital layers form part of a fan-delta that are deposited during flood events emanating from the Ze'elim Wadi. These detrital layers thicken and pond on the upslope (SW) side of the concretions where they are also at a higher level (Fig. 9a-c). This suggests that concretions may have protruded slightly above the general level of the lake floor and thereby influenced deposition of sediment. Thirdly, brecciated horizons and slump folds are preferentially developed and thickened on the downslope (NE) side of the concretions, suggesting some slumps initiated or flowed off the evaporites that formed bathymetric 'highs' (Fig. 9a, b, d). Slump folds developed downslope of evaporite mounds may also suggest that flow accelerated over the mound, and then subsequently decelerated downslope leading to contraction and folding. Fourthly, minor unconformities are locally developed above rotated beds developed around the flanks of evaporite concretions (Fig. 9e-g). Such unconformities are similar to the stratigraphic breaks that bound

halokinetic sequences that form during growth of passive salt diapirs on a regional scale (e.g. Giles and Rowan, 2012; Alsop et al., 2016b).

In addition to the observations supporting syn-sedimentary growth of concretions noted above, there is also evidence for continued growth of evaporite concretions following sedimentation around them (i.e. post-sedimentary growth). Firstly, evaporite concretions affect multiple slumps at different stratigraphic levels, and were therefore actively growing both during slumping, and the time interval between slumps (Fig. 9a-c). Secondly, beds are rotated to sub-vertical attitudes on the flanks of concretions and would be highly unstable if not buried by overlying beds (i.e. bed rotation must have continued after deposition of overlying sediments) (Fig. 9e). Thirdly, slump folds are tilted upslope along the flanks of concretions and are reworked by later folds verging off the crests of concretions (Fig. 9d). Fourthly, slump fold hinges and limbs are attenuated as they are stretched and arched over the crest of the growing evaporite concretions (Fig. 9c, h, i). Fifthly, reverse faults that develop off the crest of evaporite concretions crosscut and offset attenuated limbs of slump folds, thereby demonstrating the continued growth of evaporite following slumping (Fig. 9e, f).

7. Wooden fragments incorporated into the slump

We analyse the orientation of wooden fragments and sticks that are embedded within the detrital beds that subsequently were involved in downslope slumping (Figs 3a, d, 10a, b). The wooden sticks were presumably washed in during wadi flash flood events that also deposited the detrital beds. Longer sticks (>10 cm exposed) are frequently parallel to adjacent fold hinges, suggesting that they influenced flow and created perturbations around which folds nucleated (Fig. 10a). However, shorter wooden fragments are typically sub-parallel to flow as defined by the dip direction of beds (Figs 3a, 10b). On the NW side of the gully, wooden sticks (and fold hinges) are clockwise (285°) of short wooden fragments (242°) that are sub-parallel to flow, whereas on the SE side of the gully the long wooden sticks are anticlockwise (039°) of wooden fragments (047°) and the flow direction (Fig. 10c). The overall wooden fragments (mean 054°) are sub-parallel to flow (042°), suggesting that they rotated during transport in a manner similar to ‘pooh-sticks’ (Milne, 1928) thrown into a stream.

8. Discussion

8.1. What triggers slumping and does it reflect creep or catastrophic slope failure?

The Ze’elim Formation comprises alternating aragonite-rich and detrital-rich laminae that form couplets similar to those observed in the underlying Lisan Formation. (Figs 2k, 10d). Based on a unique match between two independent earthquake records (i.e., one historical and one derived from breccia layers in core), Agnon et al. (2006 p. 206) conclude that the lamination is seasonal with a detected annual cycle. Detrital-rich laminae may represent sediment washed into the basin during wadi flood events most likely to occur in the winter, whereas the aragonite laminae precipitate out of the upper surface waters of the Dead Sea mainly during hot summer months (e.g. López-Merino et al., 2016). An age model for the Ze’elim Formation for the last ~2,500 yr (Ken-Tor et al., 2001) suggests a relatively uniform rate of sedimentation of 0.5 cm/yr during three periods, separated by two hiatuses between 400 and 1200 A.D., and 1300 and 1750 A.D. However, in the studied section itself, there is no evidence for significant unconformities and marked breaks

in sedimentation are therefore unlikely. The aragonite- and detrital- rich couplets therefore broadly represent varves that may be approximated to annual cycles (e.g. Ben-Dor et al. 2019) and may therefore be used to estimate periods of time between slump events in the studied section. Within the case study, counting of varves suggests 18 cycles within the slump itself, and a further 15 cycles below this slump and above the underlying slumped horizon (Fig. 2k). There would therefore be approximately 33 years between slump events. This is unlikely to record large or even moderate (M>5.5) earthquake triggers as the seismic recurrence interval for moderate earthquakes in the Dead Sea area during the Holocene is estimated as ~100 to 300 years (Ken-Tor et al., 2001). In detail, Agnon et al. (2006) demonstrate that shortly before the end of the 10th century A.D., the recurrence interval inferred from seismogenic breccias layers created by M>5.5 earthquakes decreases from 95 to 50 years. The recurrence interval then increases back to a medium level of 74 years during the 14th century A.D. In general, the earthquake recurrence intervals are therefore too long to create the repeated slope failures that are observed in the section. While there is some discussion of whether detritus and aragonite laminae may both be deposited during the rainy season (e.g. López-Merino et al., 2016), the net effect of any miscounting would actually be to reduce the interval between slump events even further. It is therefore more likely that slope failure is triggered by relatively small (M<5) earthquakes or other sea-floor processes linked to steeper (5° to 10°) slopes that are inherently unstable.

Slope failure associated with MTDs may in general vary between creep that takes place over a number of years, to catastrophic landslips that are geologically instantaneous (e.g. see Ortner and Kilian, 2016). There are a several lines of evidence that may be used to help ascertain rates of movement in the case study.

8.1.1. Concretion growth affects fold geometries

Evaporite concretions affect sedimentation and slumps through several stratigraphic packages, indicating that concretions continued to grow over a period of time (Fig. 9a-c). In particular, we note that the wavelength and amplitude of slump folds dramatically increases as they pass over the crest of concretions (Fig. 9c, h). The fold amplitude of a marker horizon cannot have been increased by an order of magnitude from an average of 6.5 cm amplitude away from the concretion to 65 cm amplitude over the crest by later concretion growth alone (Fig. 9c, h). We suggest that as these folds were amplifying they must also have been stretched by concretion growth i.e. the slump process may have been relatively slow. In addition, the observation that slump folds verge both towards and away from concretions up locally tilted beds indicates that there has also been a component of bed rotation after slumping, during continued concretion growth (Fig. 9d, e). In some instances, slump fold geometries are modified by evaporite concretions such that folds that are rotated on the flanks of concretions are more open and less sheared than folds in the same horizon a few centimetres away (Fig. 9h, i). This ‘strain shadow’ effect shows that the concretion was directly influencing the slump process, before rotating slumps into steeper attitudes during continued growth. It is unlikely that the slump process was geologically instantaneous if concretion growth was able to cause lateral strain gradients during the actual slump process.

Although the absolute rates of gypsum nucleation and crystal growth kinetics from the northern Dead Sea are unknown, they are thought to be relatively slow when compared with similar

brine solutions from elsewhere (Reznik et al., 2009; Warren, 2016, p.364). This is attributed to the low solubility of gypsum which reflects the high Ca2+/SO4 2− molar ratio (115), the high salinity (≈280 g/kg) and to Na+ inhibition in the waters of the Dead Sea (Reznik et al. 2009; Warren 2016, p.364). In summary, while the rate of concretion growth in the studied section remains unknown, the structural and stratigraphic relationships indicate that concretions grew during slope failure. The extreme attenuation of bed thicknesses, coupled with dramatic increase in fold amplitude, and variation in fold geometry adjacent to concretions suggests a relatively slow slump fold process

8.1.2. Lack of sedimentary caps and infilling of synformal depressions

Slumps within the Lisan Formation that surrounds the Dead Sea (Fig. 2b) are typically overlain by a thin sedimentary 'cap' that infills local erosive scours and thins over topographic 'highs' (e.g. Alsop et al., 2020c, d). This cap, which is usually < 10 cm thick, comprises mixed aragonite and detrital sediment that may display grading. The cap was probably deposited out of suspension in the immediate aftermath of a slope failure event (Alsop and Marco, 2012b; Alsop et al., 2016a). For sediment to be thrown into suspension indicates rapid slope failure potentially, although not exclusively, linked to seismicity. Within the Ze'elim case study however, there is a notable lack of sedimentary caps overlying the slumped horizon, with overlying sediments directly infilling irregular slump topography, suggesting that caps could not have been subsequently removed by erosion (e.g. Figs 6e, 10a, b). We propose that sediment did not enter the water column and slope failure may therefore have been relatively slow and potentially linked to downslope creep rather than seismically-triggered catastrophic failure.

Within the case study slump, antiforms and synforms are draped by overlying laminae that thin over antiformal crests and thicken into synformal depressions to infill local topography created by the slump (e.g. Fig. 10a). A number of beds above the slump may display this thickening and thinning suggesting that the 'ponding' of sediment took place over a period of years. This also demonstrates that slumps were operating at the surface. The observation that wooden fragments are sub-parallel to the flow direction within normally more competent detrital-rich layers, as demonstrated by detrital layers displaying parallel fold shapes (Alsop et al., 2020d), indicates that slumping was slow enough to allow physical rotation to take place without disruption of adjacent laminae (Fig. 10b). In summary, although unconformities may locally form above the slumped horizon (e.g. Fig. 10 a, b), the lack of a sedimentary cap, together with progressive infilling of structural topography by overlying beds, is consistent with downslope creep of surficial slumps.

8.1.3. Unconformities affected by later thrusting.

Within a slumped horizon adjacent to the case study, unconformities that overlie the slump are themselves cut by thrusts further upslope (Fig. 10e, f). This suggests continued movement of the slump after the unconformity formed, as overlying sedimentary packages are progressively affected by thrusts. Reactivation of thrusts and/or formation of new thrusts that cut younger overlying unconformities is entirely consistent with continued downslope creep of a slump.

In summary, the development of slumps at approximate 30-year time intervals is consistent with slope failure potentially triggered by relatively small earthquakes linked to steeper (5° to 10°) slopes that are inherently unstable. The observation that slump fold geometries were modified as they

form by growth of concretions, together with a lack of sedimentary caps, infilling and ponding of overlying sediments, and thrusts cutting overlying unconformities all support relatively slow downslope creep of the slump. Additional supporting evidence for slow downslope movement includes the absence of normal faults towards the upslope head of the slump where they would normally be expected to occur (e.g. Farrell, 1984). Slower strain rates associated with creep have permitted extension to be accommodated by attenuation of water-rich beds rather than distinct faults and fractures.

8.2. How reliable are different methods of determining palaeoslope?

Given that the modern slope is fully exposed due to the rapid fall in water levels in the Dead Sea, this case study represents an ideal opportunity to test how reliable different methods of palaeoslope analysis are. Although bedding typically forms parallel to the slope, such that the strike of bedding is parallel to the trend of the slope while the dip direction is directly down the slope (e.g. Jones, 1939), this relationship may be complicated by later faulting and folding associated with tectonics (e.g. Sharman et al., 2015). In the present study, the lack of later tectonics affecting these modern slumps enables the mean dip-direction of bedding to act as a direct gauge of slope direction (042°) and becomes a reference datum against which the trends of clockwise and anticlockwise fold hinges and axial-planar strike may be directly measured and compared (Figs 3a, d, 7c, 8a, b). The observation that the mean dip direction of bedding (042°) is slightly anticlockwise of the mean flow direction calculated from structural analysis (050°) and wooden fragments (054°) may reflect the fact that gully 3 is located on the northern side of the Ze'elim fan (Figs 2b, c 3d). The dip direction of bedding is expected to vary systematically around this lobe, while the slump flow direction may be controlled further upslope and reflect the bulk geometry of the sediment lobe. The dip direction of bedding would therefore be expected to be slightly anticlockwise of MTD flow on the northern side and clockwise of flow on the southern margin of the fan. The bedding dip systematically increases down the axis of the lobe, from 1° to 2° further west up the fan, to 5° to 10° at the eastern extent where slope failure is triggered to create the studied slump horizon.

8.2.1. Mean Axis Method (MAM)

While fold hinges are features of folds that may be directly measured in the field, fold axes are defined as the "statistical averages of the trends of several fold hinges" (e.g. Powell, 1992, p.66), and as such are used in many arithmetic methods of palaeoslope analysis. Fold hinges are traditionally considered to form at high angles or normal to the downslope direction, and thereby form a statistical mean grouping of fold axes parallel to the strike of the slope and at right angles to the dip direction of the slope (Jones, 1939). This mean axis method (MAM) is perhaps the geometrically simplest of techniques to determine orientations of palaeoslopes, and hence the direction of gravity-driven mass flow (see Woodcock, 1979; Strachan and Alsop, 2006; Alsop and Holdsworth, 2007; Debacker et al., 2009; Alsop and Marco, 2012a; Sharman et al., 2015, 2017). Complications to this methodology are developed where fold axes have rotated towards the downslope direction during continued progressive deformation, or when folds are actually created sub-parallel to downslope flow directions during LNS (see Alsop and Marco, 2012a, Table 2). If MAM was strictly applied to the present study, then interpreted flow directions on the SE side of the gully would vary from the east to SE as we move progressively up the slump profile, whilst flow directions on the NW side of the gully vary from the

NE to the NW (Figs 3a, e, f, 4a-k, 5a-j). A consequence of this variation is that application of MAM on each side of the gully indicates flow directions that are more than 90° apart (359° and 104°) (Fig. 11a, Table 3). However, if we take the overall mean from both sides of the gully then MAM suggests flow towards 051° which is broadly parallel to the 042° downslope direction recorded by bedding (Figs 3a, g, 11a, Table 3).

8.2.2. Mean Axial Plane Strike method (MAPS)

This technique utilises the mean strike of fold axial planes (rather than fold axes) to determine the flow direction and has been used by a number of authors in both metamorphic rocks (e.g. Alsop and Holdsworth, 2007) and MTDs (e.g. Strachan and Alsop, 2006; Debacker et al., 2009; Alsop and Marco, 2012a; Sharman et al., 2015; Alsop et al., 2016a; Jablonska et al., 2018). The method assumes that fold axial planes strike parallel to the trend of the palaeoslope and will generally dip in the upslope direction (see Woodcock, 1979) (Table 2). As with the mean axis method (MAM), complications to the methodology are introduced when axial planes are either rotated during progressive downslope flow, or are created oblique to the dip direction during differential downslope shear (LNS) (Table 2). If MAPS were applied to the SE side of the gully then interpreted flow varies from due east to SE as we move up the slump profile, while interpreted flow on the NW side of the gully progressively changes from NE to NW (Figs 3a, e, f, 4a-k, 5a-j). Once again, the calculated flow direction using MAPS is > 90° apart for each side of the gully (002° and 101°), while the overall mean when data from both sides of the gully are combined is 051° (Fig. 11b, Table 3).

8.2.3. Mean Axial-planar Dip method (MAD)

This method is based on the assumption that steeper axial planes and their associated fold hinges have undergone less rotation during progressive sub-horizontal shearing and therefore more closely preserve their original orientation and vergence (e.g. Alsop and Marco, 2012a; Sharman et al., 2015; Alsop et al., 2016a; Jablonska et al., 2018). The technique examines the strike of steeper axial planes (dipping >45° with respect to bedding) and the trend of their associated fold hinges, with the hypothesis that they form at right-angles to the flow direction in LPS (Table 2). The MAD method therefore differs from MAM in that only steeper axial planes and related fold hinges are analysed, rather than all folds as in the case of MAM. However, the MAD method may become compromised in LNS-dominated settings in both metamorphic rocks (e.g. Alsop and Holdsworth, 1993; 2007) and MTDs (e.g. Debacker et al., 2009) where it is suggested that steeper axial planes will form sub-parallel (rather than normal) to flow with poles to axial planes creating stereographic girdle patterns that arc about the transport direction. If the MAD method is applied to the SE side of the gully, interpreted flow varies from 093° (hinges) to 091° (steep axial plane), while the NW side of the gully is marked by interpreted flow towards 008° for both hinges and axial planes. (Fig. 11c, d, Table 3). If we combine the MAD method data from both sides of the gully then MAD (hinges) suggest flow towards 051°, while MAD (axial planes) indicates flow to 049° (Table 3).

8.2.4. Separation Arc Method (SAM)

The Separation Arc Method (SAM) of Hansen (1971) relies on variable attitudes and geometries of folds around the slope direction. This technique is based on the assumption that groups of folds

displaying opposing vergence and differing orientations develop during variable LNS, and are symmetrically bisected by the downslope flow direction (e.g. Hansen, 1971; Lajoie, 1972; Woodcock, 1979; Strachan and Alsop, 2006; Sharman et al., 2015, 2017) (Table 2).

One of the main weaknesses of the SAM is that it is reliant on recording the end-member fold hinge orientations for each set of opposing (S or Z) vergence folds (Table 2). Clearly this is highly dependent on sampling of folds and therefore on quality, extent and access to outcrop across the slump. Given the extreme measurement and sampling procedure of folds in this study, it should be ideally suited to the SAM and provide a reliable estimate of flow direction. If we take mean fold hinge orientations for each 2.5 m section of the slump profile, then the extreme hinge orientation for the east and SE-verging folds in the SE gully and NE and NW verging folds in the NW gully trend 035° and 045° respectively, meaning that the symmetrical bisector (flow) is towards 040° (Fig. 11e, Table 3). If we take individual SE and NW-verging folds from each side of the gully, then the extreme hinge orientation plunges towards 220° in each case, also precisely constraining the SAM flow direction towards 040°. When SAM is examined down the length of the slump profile by using means from each 5 m section, then two trends emerge; a) the separation arc increases down the slump profile from 5° at 20 to 25 m to 71° at the toe (0 to 5 m), despite increasing amounts of data towards the toe that might be expected to reduce the data separation arc; b) there is progressive swing in the bisector trend (flow) from 038° at 20 to 25 m to 061° at the toe (0 to 5 m) (Table 4). This may reflect the fact that fold hinges do not need to be symmetrically disposed about the bisector, and the true flow direction only needs to be situated somewhere between the fold end members. In other words, the overall 040° bisector always lies within the separation arc of all the data subsets and may be closer to the true flow direction than an artificial bisector that assumes symmetrical flow.

8.2.5. Facing Azimuth Bisector (FAB)

Fold facing provides a directional notation that is assumed to broadly parallel the flow direction in a simple LPS scenario where facing (and vergence) are assumed to be directly downslope (e.g. Woodcock, 1976a, b). However, during differential LNS, facing directions form oblique or at right angles to the true flow direction in both metamorphic rocks (e.g. see Alsop and Holdsworth, 2007) and MTDs (e.g. Alsop and Marco, 2012a; Alsop et al., 2016a). Where a range of fold vergence and facing directions are created around an arc of fold orientations, the Facing Azimuth Bisector (FAB) parallels the flow direction. This technique may therefore be most sensitive to flows marked by combinations of LPS and LNS that would collectively create such an arc of orientations. In the case study, mean fold facing from the SE side of the gully is towards the SE (105°), whereas facing from the NW side of the gully is towards the north (359°), meaning that the overall bisector (FAB) is towards 056° (Table 3). When FAB is examined in detail down the length of the slump profile by using means from each 5 m section, then two trends emerge: a) the facing arc decreases down the slump profile from 152° at 20 to 25 m to 66° at the toe (0 to 5 m); b) there is a progressive slight swing in the FAB trend (flow) from 043° at 20 to 25 m, to 056° at the toe (0 to 5 m) (Figs 3a, g, 11f, Table 5).

8.2.6. Axial-planar Intersection Method (AIM)

The Axial-planar Intersection Method (AIM) uses the mean orientation of fold axial planes to determine the flow direction in metamorphic rocks (e.g. Alsop and Holdsworth, 2007) and MTDs (e.g. Strachan and Alsop 2006; Debacker et al., 2009; Alsop and Marco, 2012a; Sharman et al., 2015, 2017;

Sobiesiak et al., 2017). Within pure LPS systems, the mean intersection of axial planes forms normal to the flow direction, which can be ascertained by the orientation of axial planes that typically dip up the slope as folds verge down the slope (Table 2) (Alsop and Marco, 2012a, p.101). Alternatively, in pure LNS settings axial planes of oppositely verging (S and Z) folds will intersect parallel to the flow direction (Table 2) (see Alsop and Holdsworth, 2007; Alsop and Marco, 2012a, p.101). In many systems however, a combination of LPS and LNS components results in axial planes typically dipping up the slope and generally fanning around the flow direction. In such 'mixed' LPS and LNS settings, the intersection of axial planes is typically parallel to the downslope flow direction. In the case study, the bulk AIM provides an estimate of flow towards 044° (Figs 3a, g, 11g, Table 3). If we restrict our analysis to steeper axial planes dipping >45° (see description in MAD method above) then the estimate of flow is towards 058° (Fig. 11h, Table 3). When we look at how AIM varies down the slump profile, we find only limited variation apart from 10 to 15 m where the AIM direction becomes more ENE trending and may reflect sampling of the increased number of double-verging box folds in this part of the section (Figs 3a, g, 4e-g, 5e-g, 6d-f).

In summary, when complete data sets are analysed then palaeoslope methods generally produce estimates within 10° of one another (Table 3), suggesting that they are robust measures of transport direction. However, where partial data sets are used then estimates of flow may vary significantly on either side of the gully despite being <10 m apart.

8.3. What kinematic models best explain fold geometries in MTDs?

Data from the case study show that: a) bedding dip directions are broadly constant towards the NE along each slump profile on either side of the gully (Fig. 3a); b) wooden fragments are broadly parallel towards the NE in each slump profile on either side of the gully (Figs 3a, 10a-c); c) calculated normals to mean fold hinges, bisectors of fold facing, and fold axial plane intersections are broadly parallel towards the NE in each slump profile on either side of the gully (Figs 3a, g, 11a-h); d) the toe of the slump on each side of the gully passes laterally downslope into undeformed beds with no evidence of becoming emergent and creating radial flow directions (Fig. 6a, b). Collectively, these observations indicate that the flow direction is constant, and models associated with significant components of radial spreading and variable flow directions often associated with emergent toes (Fig. 1a, b) can be discounted.

This leads us towards the two potential models in which the flow direction is constant, while flow velocity is either relatively uniform along strike thereby creating LPS (Fig. 1c), or alternatively, flow velocity is variable along strike leading to differential LNS (Fig. 1d). We now examine each of these end member scenarios in relation to data and observations from the case study.

8.3.1. Layer-parallel shear

LPS is generated where flow along a detachment has a relatively constant velocity along strike (Figs 1c, 12a). The resulting downslope-verging folds display gently-curvilinear hinges that arc around flow-parallel culmination and depression surfaces (Fig. 12a) (Alsop and Holdsworth 2007). Axial-planar strike also varies systematically around the flow direction, while associated dip directions are broadly upslope (e.g. Woodcock 1976a, b: 1979). This results in folds generally facing in the downslope direction (Fig. 12a). During continued LPS, folds may progressively rotate towards the

flow direction, with hinges originally trending anticlockwise of flow undergoing clockwise rotation, while clockwise trending hinges are subject to anticlockwise rotation (Fig. 12a). Rotation is associated with tightening of fold hinges as axial planes also rotate and flatten into the sub-horizontal shear plane. A consequence of fold rotation is that angles of hinge pitch on axial planes typically increase as folds become increasingly curvilinear to create sheath fold geometries during intense shear (e.g. Alsop and Holdsworth, 2007).

Within the case study, there is no significant tightening of folds (or increase in % contraction) in areas where folds are sub-parallel to the flow direction further up the slump profile (Figs 4a-k, 5a-j, 7b). This suggests that folds have not rotated (and tightened) into their present attitudes. In addition, rotation of fold hinges to create sheath folds leads to increasing values of hinge pitch on associated axial planes (e.g. Strachan and Alsop, 2006; Alsop and Holdsworth 2007). However, in the case study, the strike of fold axial planes and trend of fold hinges both vary systematically with one another (Fig. 7g, Table 1) meaning that no such relationships in angles of pitch exist. Rotation of fold hinges in steeply-dipping axial planes would result in fold hinges becoming more steeply plunging. However, while some fold hinges display a gentle curvilinearity associated with steep axial planes (e.g. Fig. 6c), there is a general lack of steeply plunging hinges. In addition, the preservation of steep axial planes suggests that hinges were not significantly rotated; otherwise axial planes would have flattened into the sub-horizontal plane of flow. In summary, the geometric relationships in the case study do not support an LPS 'sheath fold' model to rotate fold hinges towards the flow direction. However, local areas towards the toe of the slump, where fold hinges and axial planes preserve higher angles to flow (e.g. Figs 3a, 7c, 8a, b), may represent a domain with a greater LPS component.

8.3.2. Layer-normal shear

LNS is generated where flow along a detachment has a variable velocity along strike (Figs 1d, 12b). The component of differential shear results in cylindrical fold hinges that form oblique (<45°) or sub-parallel to the downslope flow direction (Fig. 12b). LNS folds verge and face around flow-parallel culmination and depression surfaces that represent localised cells or 'lobes' of relatively rapid 'surging' and slower 'slackening' flow respectively (Alsop and Holdsworth, 2007) (Figs 1d, 12b). Differential sinistral LNS generates fold hinges and associated axial planes that trend clockwise of flow (and display Z geometries viewed towards flow), whereas dextral LNS creates fold hinges and axial planes that trend anticlockwise of flow (and display S geometries viewed towards flow) (Fig. 12b) (e.g. Alsop and Holdsworth 2007). Two distinct fold trends are thereby created that typically verge and face at high angles to the downslope direction (Fig. 12b). Fold hinges generated during LNS only undergo limited rotation during progressive deformation as high shear strains are required to rotate sub-parallel hinges into the flow direction. LNS therefore typically creates oblique asymmetric folds with stretching along hinges (e.g. Coward and Potts, 1983). As axial planes also lack notable rotation, then sub-horizontal fold hinges trend parallel to axial planar strike, and the relatively low angles of hinge pitch on axial planes are preserved (e.g. Alsop and Holdsworth, 2007).

Within the case study, folds lying oblique or sub-parallel to flow typically display hinge-parallel stretching leading to cylindrical fold hinges (e.g. Fig. 6e, f). Folds that are anticlockwise of flow on the SE gully display vergence to the east and SE, whereas clockwise folds on the NW gully show opposing NE and NW vergence (Fig. 3a-f). This pattern is consistent with differential shear generating clockwise and anticlockwise folds with two distinct hinge trends marking sinistral and

dextral LNS respectively. This is corroborated by wooden sticks (and adjacent fold hinges) that are clockwise of shorter wooden fragments that are sub-parallel to flow on the NW side of the gully, whereas on the SE side of the gully the long wooden sticks are anticlockwise of wooden fragments and the flow direction (Fig. 10c). This pattern supports anticlockwise rotation (wooden sticks disintegrating to fragments) associated with sinistral shear on the NW side of the gully, and clockwise rotation of sticks generated by dextral differential shear on the SE side.

There is a relative lack of SE-trending hinges and axial planes on either side of the gully, apart from at the toe on the NW side (Figs 3a-f, 5a, b). Such SE-trending hinges would be at high angles to the walls of the gully and would therefore presumably have been sampled if they existed further up the slump profile. This relative absence of SE-trending hinge data is significant as this is the fold orientation from which sheath folds would have originally developed during LPS, but a lack of such flow-normal folding is to be expected in LNS-dominated settings. The systematic variation of sub-horizontal fold hinge trends and their axial-planar strike (Fig. 7g) means that there is no increase in hinge pitch on axial planes, and once again is as predicted in the LNS model.

In summary, the LNS model best fits most of the observations, with folding anticlockwise of flow suggesting differential sinistral shear along the NW gully, whereas folding clockwise of flow supports differential dextral LNS on the SE side of the gully. However, at the toe of the slump fold hinges are developed at greater angles (>45°) to the flow direction and suggest a potential LPS component that is now discussed further.

8.4. How do LPS and LNS components vary along the length of a slump profile?

At the toe of the slump, the trends of fold hinges and axial planes from the SE gully are > 40° anticlockwise of the flow direction (042°), while fold hinges and axial planes from the NW gully are > 70° clockwise (Table 1). These relatively high obliquities, coupled with the downslope vergence, facing directions within 35° of flow, and development of thrusts (Fig. 6a-d, Table 1) are all consistent with a greater LPS-dominated component of deformation at the toe (Alsop and Holdsworth, 2007; Alsop et al. 2018) (Figs 12a, 13a, b, 14). As structures are traced up the slump profile towards the head, the trends of fold hinges and axial planes from the SE gully progressively decrease to <10° anticlockwise of the flow direction (042°), while fold hinges and axial planes from the NW gully are <5° clockwise (Table 1). This progressive swing in fold trends is also associated with opposed vergence and facing directions on either side of the gully that are at high angles (>80°) to the slope direction, and consistent with a greater component of LNS towards the head (Figs 12b, 13a, b, 14) (see section 8.3. above). Reversals in fold vergence and fold facing directions define culmination surfaces that bisect the overall ‘lobe’ and are parallel to downslope flow above a basal detachment (Figs 12a, b, 14).

In the case study, the greatest amount of shortening (~35%) is recorded by folds and thrusts generated by LPS affecting marker horizons at the toe of the slump, and this progressively diminishes upslope towards the head. We have already noted that such estimates of shortening may be complicated by the effects of early layer-parallel compaction, or later modification of buckle fold geometries during progressive shear. Whilst it could also be argued that a reduction in shortening up the profile simply reflects increasingly oblique cuts of the gully walls across variable fold hinges, care was taken to examine folds in 3-D in order to generate true profiles. The fold geometries themselves become more open further up the slump profile broadly supporting a reduction in shortening towards

the head (Figs 4a-k, 5a-j). The gentle dip of axial planes near the toe itself may also be a consequence of increased LPS, while some steeper axial planes further up the slump profile towards the head record greater LNS components (Fig. 6a, b). The observation that most shortening occurs at the toe is consistent with general models of slumping (e.g. Fossen, 2016). Greater amounts of shortening at the toe may reflect a larger proportion of 'lock up' strain created during cessation of movement that initiated at the toe and then progressively migrated back up slope (anti-dislocation cell of Farrell, 1984). The variably dipping and steep axial planes that are associated with 'box fold' geometries in the central portion of the slump profile (5 to 15 m from the toe) may be linked to such cessational strain and correspond to a thickening of the slump sheet (Fig. 6c-f). In addition, box folds appear to locally refold earlier structures such as tight folds and thrusts, suggesting that there may be a component of late-stage contraction (Figs 6e, 10d). The observation that pairs of box fold hinges maintain parallelism to one another on each side of the gully, but are oblique to their counterparts on the opposite side of the gully, suggests that cessational strain mirrors the earlier patterns of folding created during LNS (e.g. Fig. 6d-f).

The reality is therefore one in which LPS and LNS are simply end-members in a broad spectrum of possible shearing scenarios (Fig. 14). Variable components of LPS-dominated and LNS-dominated deformation create a potential range of structures at different times and in different parts of an MTD. In the present case study, the increasing LPS component towards the toe is manifest by tighter folds and thrusts resulting in greater amounts of shortening, while increasing LNS towards the head is marked by folds trending sub-parallel to the flow direction with vergence and facing at high angles to the slope (Fig. 14).

9. Conclusions

The drop in water levels in the Dead Sea has only recently exposed a modern unconsolidated slump developed in wet sediments. This has allowed us to undertake a highly detailed analysis of this slump profile that involved more than 500 structural measurements along a freshly incised 25 m gully section. We have established four general models that are potentially capable of explaining variable fold hinge and axial plane orientations linked to flow direction and flow velocity around 'lobes' within MTDs. This analysis allows us to draw the following conclusions.

1) Counting of varves within the Ze'elim Formation suggests slumps formed at ~33 year intervals which is consistent with recurrent failure of relatively steep (5° to 10°) slopes that were inherently unstable. Modification of slump fold geometries by evaporite concretions, in association with an absence of sedimentary caps, infilling and ponding of overlying sediments in slump topography, and most significantly, thrusts cutting unconformities above slumped packages all suggest relatively slow downslope creep of the slump.

2) Direct observation of the modern slope, combined with an alignment of wooden fragments sub-parallel to flow, allowed us to test seven principal methods of estimating palaeoslope that have been previously applied in older rocks. Evaluation of complete fold data sets leads to slope estimates within 10° of one another, and the well-known techniques of palaeoslope analysis therefore appear robust. However, where only partial data sets are employed, then these techniques suggest 'palaeoslope' orientations that may apparently vary by ~180° and are up to 90° from the actual slope, despite measurements <10 m apart.

3) The various methods of palaeoslope analysis indicate that the direction of flow does not vary significantly down the slump profile and there is no evidence of radial spreading or divergent flow at the toe. Models of constant flow direction may be divided in to (a) layer-parallel shear (LPS) where along strike velocities do not vary significantly, but progressive deformation leads to rotation of fold hinges to create curvilinear sheath folds, and (b) layer-normal shear (LNS) where along-strike changes in rates of movement leads to differential shear that creates folds sub-parallel to flow around the flanks of flow lobes. The differential LNS model is most appropriate in the case study as: a) minor folds are generally cylindrical; b) folds form two distinct trends that are clockwise and anticlockwise of flow respectively, and; c) relatively few flow-normal fold hinges are observed, despite this being the necessary pre-requisite orientation for unrotated folds in the LPS sheath fold model.

4) Variable components of LNS-dominated and LPS-dominated deformation create a potential range of structures at different times and in different parts of an MTD. In the case study, increasing LNS towards the head is marked by folds trending sub-parallel to the flow direction with vergence and facing at high angles to the slope, whereas increasing LPS towards the toe is suggested by tighter folds developed at higher angles (>45°) to the flow direction resulting in a greater amounts of shortening. The generation of box folds that locally refold earlier structures suggests that some deformation is associated with cessational 'lock up' strain that propagates back up the slope when downslope movement ceases at the toe. Such extreme variability in fold measurements over relatively small (<10 m) distances shows that incomplete data from regional studies may provide incorrect estimates of palaeoslope orientations, and consequently palaeogeographic reconstructions, in the ancient rock record.

Acknowledgements

RW was supported by the Israel Science Foundation (ISF grant No. 868/17) and the Israeli government GSI DS project 40706. We thank Iyad Swaed for the drone photography and Nadav Lensky for fruitful discussion during the course of this study. We also thank Cees Passchier for efficient editorial handling and John Waldron and Lorna Strachan for constructive and detailed reviews that improved the paper.

Figures

Figure 1. Schematic models showing variable fold orientations in flow cells marking the toes of slumps created by a, b) variable flow directions (green arrows) associated with radial spreading, and constant flow directions marking c) layer-parallel shear (LPS) and, d) layer-normal shear (LNS). In addition, flow velocity may vary between being constant (a, c) and variable (b, d) where more rapid 'surging' flow forms in the centre of a flow cell. In c), earlier fold hinges may undergo either clockwise (Cw) or anticlockwise (A-Cw) rotation towards the constant flow direction, thereby reducing their apical angle.

Figure 2. a) Tectonic plates in the Middle East. General tectonic map showing the location of the present Dead Sea Fault (DSF) which transfers the opening motion in the Red Sea to the Taurus-Zagros collision zone. Red box marks the study area in the Dead Sea Basin. b) Generalised map (based on Sneh and Weinberger 2014) showing the current Dead Sea including the position of the Ze'elim gully referred to in the text. The extent of the late Pleistocene Lisan Formation and the Holocene Ze'elim Formation are also shown (after Sneh and Rosenaft, 2019). c) Oblique drone photograph looking north along the Dead Sea shoreline and highlighting the case study Ze'elim 3 gully and position of the detailed map (Fig. 4a). Refer to Fig. 2b for general location. Position of shoreline separating different slope angles based on Lensky et al. (2014). d) Drone photograph providing map view of gully 3 and previous shorelines that create horizontal benches (refer to Fig. 2c for location). Photographs taken of detailed map area (GPS coordinates: 31.352140N 35.414941E) in March 2014,

e) looking SW up gully 3, f) looking at SE side of gully, and g) NW side of gully. Base of studied slump sheet in shown by green dotted line in each case, while A-B and C-D are provided as guides only. h) Photograph looking SW up gully 3 after a flood event in March 2015, while i) provides a close-up of the SE side of the gully in March 2015. A reference rock is arrowed to aid comparison of photographs i) with f) showing pre- and post-flood erosion. j) Photograph looking SW up gully 3 in March 2017 highlighting the amount of downcutting created by flooding (compare base of slump level with Fig. 2e). k) Detailed section through slumped horizons highlighting undeformed beds between each slump, together with the number of detrital-aragonite varved couplets in the uppermost (green) case study slump.

Figure 3. a) Drone photograph providing detailed map view of the case study area in gully 3 (GPS coordinates: 31.352140N 35.414941E, refer to Fig. 2d for position). The mean fold data for each 5 m section of the slump profiles exposed on the SE (in red) and NW (in blue) sides of the gully are shown, together with calculated mean trends of all data (green arrows), and bedding and aligned fragments of wood. Summary stereoplots showing b) all fold data from the SE side of the gully, c) all fold data from the NW side of the gully, d) combined fold data from the SE (in red) and NW (in blue) sides of the gully, together with arrows highlighting mean bedding dip direction and mean aligned wooden fragments. Stereoplots displaying fold data for each 5 m section of the slump profile exposed on e) SE side of the gully, f) NW side of the gully, g) combined data from the SE (in red) and NW (in blue) sides of the gully, together with green arrows representing trends of calculated mean normal to fold hinges, axial-planar intersections, and bisectors of fold facing. Refer to text for further details.

Figure 4. a-k) Overlapping photographic panels and associated stereoplots showing 2.5 m sections of the slump profile from the SE side of the gully (refer to Fig. 3a for location). Note that photographs from the SE side of the gully are mirrored in all figures so that NE always remains on the right-hand side of the images for consistency. The base of the slump (green), deformed yellow marker bed, top of slump (magenta), together with underlying and overlying orange marker beds are shown in each case. Approximate distance from the toe (0 m) to the head of the slump (25 m) is also shown. Associated stereoplots show data (in red) for each 2.5 m section and highlight the swing in folds and associated facing directions along the slump profile.

Figure 5. a-j) Overlapping photographic panels and associated stereoplots showing 2.5 m sections of the slump profile from the NW side of the gully (refer to Fig. 3a for location). The base of the slump (green), deformed yellow marker bed, top of slump (magenta), together with underlying and overlying orange marker beds are shown in each case. Approximate distance from the toe (0 m) to the head of the slump (25 m) is also shown. Associated stereoplots show data for each 2.5 m section and use the same symbols (in blue) as explained in Fig. 4.

Figure 6. Pairs of photographs and associated stereoplots of individual structures developed on the SE and NW sides of the gully (see Figs 4, 5). Base of slump (in green) and yellow marker horizon are generally shown. Structures from the toe area of the slump exposed on a) the SE side of the gully, and b) NW side of the gully. c) Gently-curvilinear fold hinges associated with steep axial planes on the SE side of the gully, with the inset photograph showing and oblique view towards the west. d) Upright box fold geometries with axial planes dipping in opposing directions on the NW side of the gully. e) Upright box fold geometries with axial planes dipping in opposing directions on the SE side of the gully. Note the cylindrical fold hinges and refolding of earlier folds. f) Cylindrical box folds with axial planes dipping in opposing directions on the NW side of the gully. Approximate distances from the toe of the slump are shown in each case and correlate with the slump profiles shown in Figs 4, 5, while the 10 cm chequered rule provides a scale. On stereoplots, fold hinges (solid circles), mean fold hinges (open circles), poles to axial planes (solid squares) and mean axial planes (great circles) are shown from the SE (in red) and NW (in blue) sides of the gully. In d, e, f), mean axial planes that dip in opposing directions around box folds are shown.

Figure 7. Graphs of structural parameters measured from the toe (0 m) to the head (25 m) of the slump profile. In each case, data from the SE gully is shown by red circles and data from NW gully in blue squares, with approximate best-fit curves shown for guidance in some cases. a) Thickness of slump sheet (see Figs 4, 5). b) Trends of fold hinges. c) Trends of fold hinges measured relative to 042° slope which acts as datum (marked as '0'). d) Acute angle between mean fold hinge trends over 2.5 m intervals on each side of gully and at equivalent distances from the toe. e) Dip direction of fold axial planes, with f) showing mean axial plane dip directions over 2.5 m intervals. g) Trend of fold hinges compared with strike of associated axial planes and highlighting

general variation from the toe to head of the slump profile in each case. h) Mean fold hinge trends over 2.5 m intervals compared to the dip of associated axial planes and highlighting general variation from the toe to head of the slump profile in each case.

Figure 8. Bar charts of a) fold hinge trends and b) axial-planar strike, together with c) rose diagrams of fold facing from each 5 m section of the slump profile (refer to Fig. 3 for associated stereoplots). In each case, 0 m represents the toe, with data from the SE gully shown in red and data from the NW gully in blue. In bar charts, a) trends of fold hinges and b) strike of axial planes are measured relative to the 042° slope which acts as datum (marked as '0'). In addition, structural elements that are clockwise and anticlockwise of slope are recorded as +ve and -ve respectively.

Figure 9. Photographs of evaporite concretions and adjacent slumps from the SE (a-c, e-i, mirrored) and NW (d) sides of the gully. In a) the examined slump sheet thins over the evaporite concretion at 24 m from the toe (Fig. 4k) with b) providing a more detailed view of this. c) Bedding is deflected downwards beneath a concretion while fold amplitudes are increased above the concretion (position shown in a). d) Photograph from the NW side of the gully showing a concretion deflecting underlying bedding downwards, while overlying beds are arched upwards and display local slumping away from the concretion. e) Photograph and close-up (f) of local unconformities forming along tilted beds near a concretion (position shown in b). Attenuated and tilted beds are cut by later reverse faults stemming from the concretion. g) Unconformities developed adjacent to concretions resulting missing section above the concretion. h) Concretion with highly attenuated slump folds passing over the crest and stepped detrital rich layers on either side (see c) for position). i) Close-up photograph showing geometry of tilted slump folds adjacent to the concretion shown in h). Yellow notebook (23 cm long), 10 cm chequered rule and 15 mm diameter coin for scale.

Figure 10. a) Photograph of long wooden sticks parallel to fold hinges at 6 m from the toe of the slump on the NW side of the gully (see Fig. 5c). The slump is unconformably overlain by undeformed beds that infill slump topography by thickening into synformal 'lows' and thinning over antiformal 'highs'. b) Photograph of short wooden fragments parallel to the flow direction at 2 m from the toe of the slump on the NW side of the gully (see Fig. 5b). The traces of folded beds in the slump are cut by an overlying unconformity. c) Stereoplot showing the orientation of long (>10 cm) wooden sticks (solid triangles), short (<10 cm) wooden fragments (solid diamonds), with mean orientations shown by open symbols in each case. Data from the SE and NW sides of the gully are shown in red and blue respectively. Wooden sticks from the NW gully are clockwise of the slope direction (as defined by the mean dip direction of beds), while sticks from the SE gully are anticlockwise. d) Photograph showing later box folds refolding earlier tight folds and thrusts at 17.5 m from the toe of the slump on the SE side of the gully (see Fig. 4h). e) Photograph (mirrored) and close-up (f) of an adjacent slump from the SE side of the gully. The photographs highlight how unconformity 1 that overlies the slump truncates underlying folds but is itself cut by thrusts indicating continued movement. A subsequent unconformity (2) then cuts these thrusts indicating surficial slumping. 10 cm chequered rule for scale.

Figure 11. Stereoplots showing summary data used by different methods of determining flow down palaeoslopes, with calculated means from the SE and NW sides of the gully shown by red and blue arrows respectively, while overall combined means are shown by black arrows. a) Mean Axis Method (MAM) of Jones (1939). b) Mean Axial Plane Strike (MAPS) method. c) Mean Axial-planar Dip (MAD) method using fold hinges associated with steeper dipping (>45°) axial planes. d) Mean Axial-planar Dip (MAD) method using the strike of steeper dipping (>45°) axial planes. e) Separation Arc Method (SAM) of Hansen (1971). f) Facing Azimuth Bisector (FAB) method where facing azimuths are plotted around the perimeter of the stereoplot. g) Axial-planar Intersection Method (AIM). h) Axial-planar Intersection Method (AIM) using only steeper dipping (>45°) axial planes. In each case, fold hinges are shown by solid circles and mean fold hinges by open circles, while poles to axial planes (open squares) and mean poles to axial planes (solid squares) are also displayed. The trends of fold facing directions are shown by solid triangles and overall means by open triangles. In each case, data from the SE gully and NW gully are shown in red and blue respectively.

Figure 12. Schematic plan view diagrams illustrating fold hinge-lines associated with synshearing flow folds during a) Layer-parallel shear (LPS), and b) Layer-normal shear (LNS). In a), fold hinges form at high angles to the flow direction (green arrows) and undergo clockwise (Cw in red) and anticlockwise (A-Cw in blue) rotations marked by reversals in fold facing directions about the transport-parallel culmination and depression surfaces. In b), syn-shearing flow folds are generated by surging flow (large green arrow) and slackening flow (small green

arrow) separated by differential layer-normal sinistral (in blue) and dextral shear (in red). See text for further details.

Figure 13. a) Schematic flow cell superimposed on drone photograph and summary (5 m mean) data of gully 3 (see Figs 2d, 3a). Differential sinistral shear is considered to operate on the NW side of the gully, whereas dextral shear dominates the SE side of the gully. b) Plan view cartoon illustrating layer-parallel shear (LPS) at the contractional toe of a slump, and differential layer-normal shear (LNS) along the flanks. See text for further discussion.

Figure 14. Summary cartoon illustrating layer-parallel shear (LPS) dominating towards the downslope toe of a slump, while increasing layer-normal shear (LNS) forms along a basal detachment further upslope. Downslope flow is marked by (green) arrows which parallel culmination surfaces that separate domains of sinistral LNS (blue) and dextral LNS (red). Fold hinges form arcs about the culmination surface resulting in fold facing (open arrows) varying from flow-normal at the head to oblique to flow at the toe.

924 **Table 1.** Mean fold hinges and axial planes from toe of slump (0 to 2.5 m) on SE side (in red) and
925 NW side (blue) of gully. From the head to the toe of the slump, there is a general anticlockwise
926 swing in hinges and axial planes from the SE side (towards the toe) and a clockwise swing in
927 hinges and axial planes from the NW side.

928

Distance	22.5 to 25 m	20 to 22.5 m	17.5 to 20 m	15 to 17.5 m	12.5 to 15 m	10 to 12.5 m	7.5 to 10 m	5 to 7.5 m	2.5 to 5 m	0 to 2.5 m
SE Gully Hinge	6/035	2/024	1/195	5/204	2/199	4/016	1/005	7/011	6/357	2/181
SE Gully AP	044/12w	023/19w	011/53w	016/11w	003/4w	017/20w	002/48w	006/33w	175/68w	173/26w
NW Gully Hinge	5/225	2/249	1/254	2/255	2/272	2/279	3/279	4/284	4/291	0/294
NW Gully AP	043/8s	073/29s	075/45s	074/24s	092/65s	105/16s	101/19s	105/33s	122/22s	118/36s

929

930

931 **Table 2.** Assumptions and associated problems of 6 methods of determining palaeoslope from fold data.
932 Note that the Axial-planar Intersection Method (AIM) is separated into settings involving layer-parallel
933 shear (LPS) and layer-normal shear (LNS). Modified from Alsop and Marco (2012a).

934

	Mean Axis Method (MAM)	**Mean Axial Plane Strike Method (MAPS)**	**Mean Axial-planar Dip Method (MAD)**	**Separation Arc Method (SAM)**	**Facing Azimuth Biscetor (FAB)**	**Axial-planar Intersection Method for LPS (AIM)**	**Axial-planar Intersection Method for LNS (AIM)**
Assumption 1	Fold hinges will verge and face downslope	Fold hinges will verge and face downslope	Fold hinges will verge and face downslope	Fold hinges will verge in a downslope arc	Fold hinges face upwards about a downslope arc in LPS	Fold axial planes will fan and dip upslope	Fold axial planes will fan and dip about the downslope direction
Assumption 2	Flow direction is normal to the mean fold axis trend	Flow direction is normal to the mean axial plane strike	Flow direction is normal to mean fold axis trend associated with steep AP dips	Flow direction bisects acute angle between folds with opposing vergence	Flow direction bisects acute angle between folds with opposing facing	Flow direction is normal to the fanning axial planes	Flow direction is parallel to the fanning axial planes
Problem 1	Does not allow for downslope (i.e. flow parallel) fold axes	Does not allow for downslope (i.e. flow parallel) fold axes and axial planes	Does not allow for downslope (i.e. flow parallel) fold axes and axial plane	Does not allow for overlapping fold distributions	Fold facing in purely LNS settings will be at high-angles to the slope	Requires careful 3-D evaluation of folding	Requires careful 3-D evaluation of folding
Problem 2	Skewed distributions not differentiated by means	Skewed distributions not differentiated by means	Skewed distributions not differentiated by means	Based on extreme end-member fold orientations	Skewed distributions not differentiated by means	Unimodal axial planar dip distribution requires even sampling	Bimodal axial planar dip distribution requires even sampling

935

936

Table 3. Mean fold hinge and axial-planar (AP) orientations with calculated slump transport directions (TD) for the SE Gully (red) and NW Gully (blue). The overall mean transport direction is given along the base of the table. MAM- Mean Axis Method, MAPS – Mean Axial Plane strike method, MAD (hinge) – Mean Axial-planar Dip method using hinges, MAD (AP) – Mean Axial-planar Dip method using axial planes, SAM – Separation Arc Method, FAB-Facing Azimuth Bisector method, AIM – Axial-planar Intersection Method, AIM (steep) - Axial-planar Intersection Method using steep (>45° dip) axial planes, Wood – aligned wooden fragments.

Method	**MAM**	**MAPS**	**MAD** (hinge)	**MAD** (AP)	**SAM**	**FAB**	**AIM**	**AIM** (steep)	**Average**	**Wood** (fragments)	**Bedding**
SE Gully (N=131)	Fold Hinge 014° (TD-104°)	Fold AP 011° (TD-101°)	Fold Hinge 003° (TD-093°)	Fold AP 001° (TD-091°)	Fold Hinge 035° (40° swing)	Facing Azimuth 105°	Fold AP 007/29W	Fold AP 001/61W (N=37)	5 methods (TD-099°)	Wooden fragment (047°)	Bedding 129/12NE (TD-039°)
NW Gully (N=130)	Fold Hinge 269° (TD-359°)	Fold AP 092° (TD-002°)	Fold Hinge 278° (TD-008°)	Fold AP 098° (TD-008°)	Fold Hinge 045° (70° swing)	Facing Azimuth 359°	Fold AP 093/28S	Fold AP 099/68S (N=54)	5 methods (TD-003°)	Wooden fragment (062°)	Bedding 134/5NE (TD-044°)
Mean	**051°**	**051°**	**051°**	**049°**	**040°**	**056°**	**044°**	**058°**	**050°**	**054°**	**042°**

Table 4. SAM from toe of slump (0 to 5 m) to upper part of slump (20 to 25 m) on SE side (in red) and NW side (blue) of gully. The bisector of the separation arc represents the flow direction.

Distance	20 to 25 m (N=18)	15 to 20 m (N=34)	10 to 15 m (N=60)	5 to 10 m (N=69)	0 to 5 m (N=63)	Extremes
SE Gully Hinge	7/035	10/220	5/210	17/032	6/205	10/220
NW Gully Hinge	5/220	1/239	2/264	1/270	3/276	5/220
Separation Arc	5°	19°	54°	58°	71°	0°
Bisector (flow)	**038°**	**049°**	**057°**	**061°**	**061°**	**040°**

Table 5. FAB from toe of slump (0 to 5 m means) to upper part of slump (20 to 25 m) on SE side (in red) and NW side (blue) of gully. The bisector of the facing arc (FAB) represents the flow direction.

Distance	20 to 25 m (N=18)	15 to 20 m (N=34)	10 to 15 m (N=60)	5 to 10 m (N=69)	0 to 5 m (N=63)	Mean trend (0 to 25 m)
SE Gully Facing	13/119	34/109	14/107	41/099	45/089	**105**
NW Gully Facing	16/327	38/344	67/007	35/012	34/023	**359**
Facing Arc	152°	125°	100°	87°	66°	**106°**
Bisector (flow)	**043°**	**046°**	**057°**	**056°**	**056°**	**056°**

References,

Agnon, A., Migowski, C., Marco, S., 2006. Intraclast breccia layers in laminated sequences: recorders of paleo-earthquakes, in Enzel, Y., Agnon, A., and Stein, M., eds., New Frontiers in Dead Sea Paleoenvironmental Research, Geological Society of America Special Publication, p. 195-214.

Alsop, G.I., Holdsworth, R.E. 1993. The distribution, geometry and kinematic significance of Caledonian buckle folds in the western Moine Nappe, northwestern Scotland. Geological Magazine 130, 353-362.

Alsop, G.I., Holdsworth, R.E. 2007. Flow perturbation folding in shear zones. In: Ries, A.C., Butler, R.W.H. & Graham, R.D. (Eds) Deformation of the Continental Crust: The legacy of Mike Coward. Geological Society, London, Special Publications, 272, 77-103

Alsop, G.I., Holdsworth, R.E. 2012. The three dimensional shape and localisation of deformation within multilayer sheath folds. *Journal of Structural Geology*. 44, 110-128.

Alsop, G.I.**,** Marco, S. 2012a. A large-scale radial pattern of seismogenic slumping towards the Dead Sea Basin. Journal of the Geological Society 169, 99-110.

Alsop, G.I., Marco, S. 2012b. Tsunami and seiche-triggered deformation within offshore sediments. Sedimentary Geology 261, 90-107.

Alsop, G.I.**,** Marco, S. 2014. Fold and fabric relationships in temporally and spatially evolving slump systems: A multi-cell flow model. Journal of Structural Geology, 63, 27-49.

Alsop, G.I., Marco, S., Weinberger, R., Levi, T. 2016a. Sedimentary and structural controls on seismogenic slumping within Mass Transport Deposits from the Dead Sea Basin. Sedimentary Geology 344, 71-90.

Alsop, G.I., Weinberger, R., Levi, T., Marco, S. 2016b. Cycles of passive versus active diapirism recorded along an exposed salt wall. Journal of Structural Geology, 84, 47-67.

Alsop, G.I., Marco, S., Levi, T., Weinberger, R. 2017a. Fold and thrust systems in Mass Transport Deposits. Journal of Structural Geology 94, 98-115.

Alsop, G.I., Marco, S., Weinberger, R., Levi, T. 2017b. Upslope-verging back thrusts developed during downslope-directed slumping of mass transport deposits. Journal of Structural Geology 100, 45-61.

Alsop, G.I., Weinberger, R., Marco, S. 2018. Distinguishing thrust sequences in gravity-driven fold and thrust belts. Journal of Structural Geology 109, 99-119.

Alsop, G.I., Weinberger, R., Marco, S., Levi, T. 2019. Identifying soft-sediment deformation in rocks. Journal of Structural Geology, 125, 248-255. doi: 10.1016/j.jsg.2017.09.001

Alsop, G.I., Weinberger, R., Marco, S., Levi, T. 2020a. Fold and thrust systems in mass transport deposits around the Dead Sea Basin. In: Ogata, K., Festa, A., Pini, G.A. (Editors). Submarine landslides: subaqueous mass transport deposits from outcrops to seismic profiles. American Geophysical Union Monograph Series. 246, p.139-154. John Wiley & Sons Inc. 384pp. ISBN: 978-1-119-50058-2.

Alsop, G.I., Weinberger, R., Marco, S., Levi, T. 2020b. Bed-parallel slip: Identifying missing displacement in mass transport deposits. Journal of Structural Geology 131, 103952

Alsop, G.I., Weinberger, R., Marco, S., Levi, T. 2020c. Distinguishing coeval patterns of contraction and collapse around flow lobes in mass transport deposits. Journal of Structural Geology 104013 doi 10.1016/j.jsg.2020.104013.

Alsop, G.I., Weinberger, R., Marco, S., Levi, T. 2020d. Folding during soft-sediment deformation. In Bond, C.E. and Lebit, H.D. (Editors) Folding and fracturing of rocks: 50 years since the seminal text book of J.G. Ramsay. Geological Society Special Publication 487, 81-104. doi.org/10.1144/SP487.1.

Armandita, C., Morley, C.K., Rowell, P. 2015. Origin, structural geometry, and the development of a giant slide: The South Makassar Strait mass transport complex. Geosphere, 11, 376-403. *doi:*10.1130/GES01077.1

Avni, Y. Lensky, N., Dente, E., Shviro, M., Arav, R., Gavrieli, I., Yechieli, Y., Abelson, M., Lutzky, H., Filin, S. Haviv, I. and Baer, G. 2016. Self-accelerated development of salt karst during flash floods along the Dead Sea Coast, Israel, J. Geophys. Res. Earth Surf., 121, 17–38, doi:10.1002/2015JF003738.

Basilone, L. 2017. Seismogenic rotational slumps and translational glides in pelagic deep-water carbonates. Upper Tithonian-Berriasian of Southern Tethyan margin (W Sicily, Italy). Sedimentary Geology 356, 1-14.

Begin, Z.B., Ehrlich, A., Nathan, Y., 1974. Lake Lisan, the Pleistocene precursor of the Dead Sea: Geological Survey of Israel Bulletin, 63, p. 30.

Ben-Dor, Y., Neugebauer, I., Enzel, Y., Schwab, M.J., Tjallingii, R., Erel, Y., Brauer, A. 2019. Varves of the Dead Sea sedimentary record. Quaternary Science Reviews 215, 173-184.

Bowman, D. 1974. River Terraces in the Dead Sea Area—Morphological Aspects. Unpublished Ph.D. dissertation, Hebrew University of Jerusalem (in Hebrew with English Abstract).

Bull, S., Cartwright, J., Huuse, M. 2009. A review of kinematic indicators from mass-transport complexes using 3D seismic data. Marine and Petroleum Geology 26, 1132-1151.

Butler, R.W.H., Paton, D.A. 2010. Evaluating lateral compaction in deepwater fold and thrust belts: How much are we missing from "nature's sandbox"? GSA Today 20, 4-10.

Coianiz, L., Schattner, U., Lang, G., Ben-Avraham, Z. 2019. Between plate and salt tectonics-New stratigraphic constraints on the architecture and timing of the Dead Sea Basin during the Late Quaternary. Basin Research DOI: 10.1111/bre.12387.

Corredor, F., Shaw, J.H., Bilotti, F., 2005. Structural styles in the deep-water fold and thrust belts of the Niger Delta. American Association of Petroleum Geologists Bulletin 89, 753-780.

Coward, M.P., Potts, G. 1983. Complex train patterns developed at the frontal and lateral tips to shear zones and thrust zones. Journal of Structural Geology 5, 383-399.

Debacker, T.N., Dumon, M., Matthys, A. 2009. Interpreting fold and fault geometries from within the lateral to oblique parts of slumps: A case study from the Anglo-Brabant Deformation Belt (Belgium). Journal of Structural Geology 31, 1525-1539.

De Lima Rodrigues, M.C.N., Trzaskos, B., Alsop, G.I., Vesely, F.F. 2020. Making a homogenite: an outcrop perspective into the evolution of deformation within mass-transport deposits. Marine and Petroleum Geology, 104033 https://doi.org/10.1016/j.marpetgeo.2019.104033.

de Vera, J., Granado, P., McClay, K. 2010. Structural evolution of the Orange Basin gravity-driven system, offshore Namibia. Marine and Petroleum Geology 27, 223-237

Enzel, Y., Kadan, G. and Eyal, Y. 2000. Holocene Earthquakes Inferred from a Fan-Delta Sequence in the Dead Sea Graben, Quaternary Research 53, 34–48 doi:10.1006/qres.1999.2096,

Farrell, S.G. 1984. A dislocation model applied to slump structures, Ainsa Basin, South Central Pyrenees, Journal of Structural Geology 6, 727-736.

Farrell, S.G., Eaton, S. 1987. Slump strain in the Tertiary of Cyprus and the Spanish Pyrenees. Definition of palaeoslopes and models of soft sediment deformation. In: Deformation of Sediments and Sedimentary Rocks (edited by Jones, M.F. & Preston, R.M.F.). Special Publication of the Geological Society of London 29, 181-196.

Fossen, H. 2016. Structural Geology. 2nd Edition. Cambridge University Press, Cambridge, UK, p.510.

Frey Martinez, J., Cartwright, J., Hall, B. 2005. 3D seismic interpretation of slump complexes: examples from the continental margin of Israel. Basin Research 17, 83-108.

Frey-Martinez, J., Cartwright, J., James, D. 2006. Frontally confined versus frontally emergent submarine landslides: A 3D seismic characterisation. Marine and Petroleum Geology23, 585-604.

Garcia-Tortosa, F.J., Alfaro, P., Gibert, L., Scott, G. 2011. Seismically induced slump on an extremely gentle slope (<1°) of the Pleistocene Tecopa paleolake (California). Geology 39, 1055-1058.

Garfunkel, Z., 1981. Internal structure of the Dead Sea leaky transform (rift) in relation to plate kinematics: Tectonophysics 80, p. 81-108.

Gibert, L., Sanz de Galdeano, C., Alfaro, P., Scott, G., Lopez Garrido, A.C. 2005. Seismic-induced slump in Early Pleistocene deltaic deposits of the Baza Basin (SE Spain). Sedimentary Geology 179, 279-294.

Giles, K.A., Rowan, M.G. 2012. Concepts in halokinetic-sequence deformation and stratigraphy. In: Alsop, G.I., Archer, S.G., Hartley, A.J., Grant, N.T., Hodgkinson, R. (Eds.) Salt Tectonics, Sediments and Prospectivity. Geological Society, London, Special Publications, 363, 7-31.

Hansen, E. 1971. Strain Facies. Springer-Verlag, Berlin, 207 pp.

Holdsworth, R.E., 1988. The stereographic analysis of facing. Journal of Structural Geology 10, 219-223.

Jablonska, D., Di Celma, C., Tondi, E., Alsop, G.I. 2018. Internal architecture of mass-transport deposits in basinal carbonates: A case study from southern Italy. *Sedimentology 65 (4), 1246-1276. doi:* 10.1111/sed.12420

Jolly, B.A., Lonergan, L., Whittaker, A.C., 2016. Growth history of fault-related folds and interaction with seabed channels in the toe-thrust region of the deep-water Niger delta. Marine and Petroleum Geology 70, 58-76.

Jones, O.T. 1939. The geology of the Colwyn bay district: a study of submarine slumping during the Salopian period. *Q. J. Geol. Soc. London*, 380, 335-382.

Kagan, E., M. Stein, A. Agnon, and F. Neumann 2011. Intrabasin paleoearthquake and quiescence correlation of the late Holocene Dead Sea, J. Geophys. Res., 116, B04311, doi:10.1029/2010JB007452.

Kagan, E.J., Stein, M., Marco, S. 2018. Integrated palaeoseismic chronology of the last glacial Lake Lisan: From lake margin seismites to deep-lake mass transport deposits. Journal of Geophysical Research: Solid Earth 123 (4) 2806-2824.

Ken-Tor, R., Agnon, A., Enzel, Y., Stein, M., Marco, S., Negendank, F.W., 2001. High-resolution geological record of historic earthquakes in the Dead Sea basin, J. Geophys. Res. 106, 2221-2234.

Korneva, I., Tondi, E., Jablonska, D., Di Celma, C., Alsop, I., Agosta, F. 2016. Distinguishing tectonically- and gravity-driven synsedimentary deformation structures along the Apulian platform margin (Gargano Promontory, southern Italy). Marine and Petroleum Geology 73, 479-491.

Lajoie, J. 1972. Slump fold axis orientations: an indication of palaeoslope? Journal of Sedimentary Petrology 42, 584-586.

Lensky N. G., Calvo R., Sade A. R., Gavrieli I., Katz O., Hall J. K., Enzel Y., Mushkin A. 2014. The Scarred Slopes of the Dead Sea – Evidence for Intensive Subsea Landsliding, Israel Geological Society Annual Meeting, En Boqeq, Abstract Volume (editor: Issachar, R.) p.81

Lopez-Merino, L., Leroy, S.A.G., Eshel, A., Epshtein, V., Belmaker, R., Bookman, R. 2016. Using palynology to re-assess the Dead Sea laminated sediments – Indeed varves? Quaternary Science Reviews 140, 49-66.

Lu, Y., Waldmann, N., Alsop, G.I., Marco, S. 2017. Interpreting soft sediment deformation and mass transport deposits as seismites in the Dead Sea depocentre. Journal of Geophysical Research: Solid Earth, 122. 10, 8305-8325. Doi: 10.1002/2017JB014342.

Maltman, A. 1994. Introduction and Overview. In: Maltman, A. (Editor) The Geological Deformation of Sediments. Chapman & Hall, London. pp. 1-35.

Manspeizer, W. 1985. The Dead Sea Rift: Impact of climate and tectonism on Pleistocene and Holocene sediments. In "Strike-Slip Deformation, Basin Formation and Sedimentation" (K. T. Biddle and N. Christie-Black, Eds.). Society for Economic Paleontology and Mineralogy Special Publication 37, 143–158.

McGee, W.J. 1891. The Pleistocene history of northeastern Iowa. Report of the U.S. Geological Survey 11, 199-571.

Milne, A.A. 1928. The house at Pooh Corner. Methuen and Company, Ltd. (London).

Morley, C.K., King, R., Hillis, R., Tingay, M., Backe, G. 2011. Deepwater fold and thrust belt classification, tectonics, structure and hydrocarbon prospectivity: A review. Earth Science Reviews, 104, 41-91.

Ortner, H., Kilian, S. 2016. Sediment creep on slopes in pelagic limestones: Upper Jurassic of Northern Calcareous Alps, Austria. Sedimentary Geology 344, 350-363.

Powell, D. 1992. Interpretation of geological structures through maps: An introductory practical manual. Longman Group UK Ltd. 176pp. ISBN 0-582-08783-X

Quennell, A. M. 1958. The structural and geomorphic evolution of the dead sea rift, Quarterly Journal of the Geological Society, 114, 1-24, doi.org/10.1144/gsjgs.114.1.0001

Reznik, I. J., Gavrieli, I., Ganor, J., 2009. Kinetics of gypsum nucleation and crystal growth from Dead Sea brine. Geochimica et Cosmochimica Acta, v. 73, p. 6218–6230.

Reis, A.T., Araújo, E., Silva, C.G., Cruz, A.M., Gorini, C., Droz, L., Migeon, S., Perovano, R., King, I., Bache, F. 2016. Effects of a regional décollement level for gravity tectonics on late Neogene to recent large-scale slope instabilities in the Foz do Amazonas Basin, Brazil. Marine and Petroleum Geology 75, 29-52.

Scarselli, N., McClay, K., Elders, C. 2016. Seismic geomorphology of Cretaceous megaslides offshore Namibia (Orange Basin): Insights into segmentation and degradation of gravity-driven linked systems. Marine and Petroleum Geology 75, 151-180.

Sharman, G.R., Graham, S.A., Masalimova, L.U., Shumaker, L.E., King, P.R. 2015. Spatial patterns of deformation and palaeoslope estimation within the marginal and central portions of a basin-floor mass-transport deposit, Taranaki Basin, New Zealand. Geosphere, 11, 266-306.

Sharman, G.R., Schwartz, T.M., Shumaker, L.E., Trigg, C.R., Nieminski, N.M., Sickmann, Z.T., Malkowski, M.A., Hourigan, J.K., Schulein, B.J., Graham, S.A. 2017. Submarine mass failure within the deltaic Domengine Formation (Eocene), California (USA). Geosphere 13, 950-973.

Sneh, A. 1979. Late Pleistocene fan deltas along the Dead Sea rift. Journal of Sedimentary Petrology 49, 541–552.

Sneh, A., Rosensaft, M. 2019. Geological Map of Israel, scale 1:250,000. Geological Survey of Israel, Jerusalem

Sneh, A., Weinberger, R. 2014. Major structures of Israel and Environs, Scale 1:50,000. Israel Geological Survey, Jerusalem.

Sobiesiak, M., Kneller, B.C., Alsop, G.I., Milana, J.P. 2017. Sub-seismic scale folding and thrusting within an exposed mass transport deposit: A case study from NW Argentina. *Journal of Structural Geology* 96, 176-191.

Steventon, M.J., Jackson, C,A-L, Hodgson, D.M., Johnson, H.D. 2019. Strain analysis of a seismically imaged mass-transport complex, offshore Uruguay. Basin Research 31, 600-620.

Strachan, L.J., Alsop, G.I. 2006. Slump folds as estimators of palaeoslope: a case study from the Fisherstreet Slump of County Clare, Ireland. Basin Research 18, 451-470.

Totake, Y., Butler, R.W.H., Bond, C.E., Aziz, A., 2018. Analyzing structural variations along strike in a deep-water thrust belt: Journal of Structural Geology, 108, 213–229.

Van der Merwe, W.C., Hodgson, D.M., Flint, S.S. 2011. Origin and terminal architecture of a submarine slide: a case study from the Permian Vischkuil Formation, Karoo Basin, South Africa. Sedimentology 58, 2012-2038.

Waldron, J.W.F., Gagnon, J-F. 2011. Recognizing soft-sediment structures in deformed rocks of orogens. Journal of Structural Geology 33, 271-279.

Warren, J.K. 2016. Evaporites: A geological compendium. 2nd Edition. Springer International Publishing, Switzerland. 1813pp.

Woodcock, N. H 1976a. Ludlow Series slumps and turbidites and the form of the Montgomery Trough, Powys, Wales. Proceedings of the Geologists Association 87, 169-182.

Woodcock, N. H 1976b. Structural style in slump sheets: Ludlow Series, Powys, Wales. Journal of the Geological Society, London 132, 399-415.

Woodcock, N.H. 1979. The use of slump structures as palaeoslope orientation estimators. *Sedimentology*, 26, 83-99.

Xypolias, P., Alsop, G.I. 2014. Regional flow perturbation folding within an exhumation channel: a case study from the Cycladic blueschists. Journal of Structural Geology 62, 141-155.

1139 Yechieli, Y., M. Magaritz, Y. Levy, U. Weber, U. Kafri, W. Woelfli,, G. Bonnani 1993. Revision of Late
1140 Quaternary geological history of the Dead Sea area, Israel, Quart. Res., 39, 59–67.

1141 Zalan, P.V., 2005. End members of gravitational fold and thrust belts (GFTBs) in the deep waters of Brazil. In:
1142 Shaw, J.H., Connors, C., and Suppe, J., (Editors) An AAPG Seismic Atlas: AAPG studies in Geology 53, 147-156.

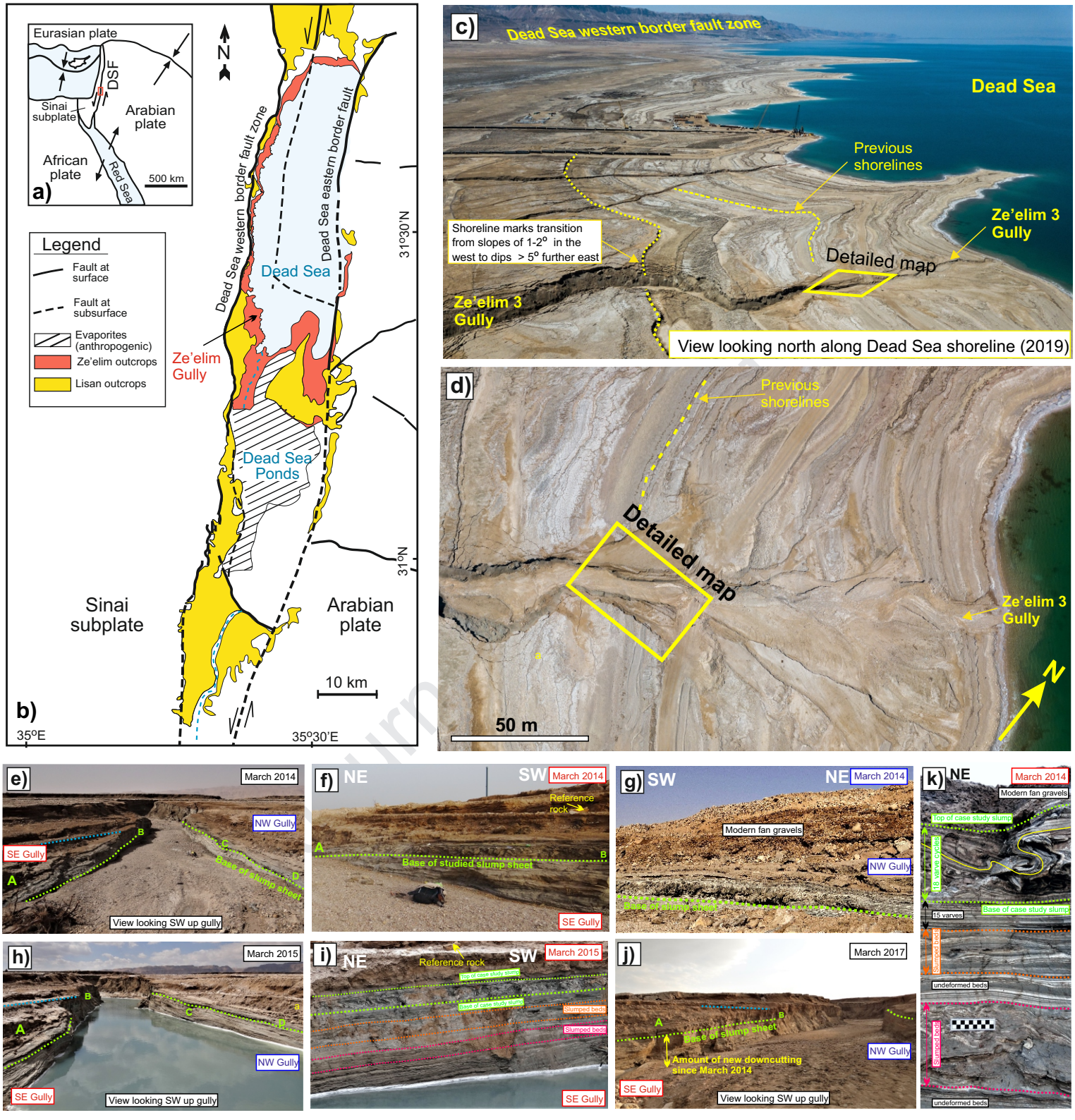
a)
Eurasian plate
DSF
Sinai subplate
Arabian plate
African plate
Red Sea
500 km
Legend
Fault at surface
Fault at subsurface
Evaporites (anthropogenic)
Ze'elim outcrops
Lisan outcrops
N
Dead Sea western border fault zone
Dead Sea eastern border fault
Dead Sea
Ze'elim Gully
Dead Sea Ponds
31°30'N
31°N
Sinai subplate
Arabian plate
10 km
b)
35°E
35°30'E
c)
Dead Sea western border fault zone
Dead Sea
Previous shorelines
Ze'elim 3 Gully
Shoreline marks transition from slopes of 1-2° in the west to dips > 5° further east
Detailed map
Ze'elim 3 Gully
View looking north along Dead Sea shoreline (2019)
d)
Previous shorelines
Detailed map
Ze'elim 3 Gully
N
50 m
e)
March 2014
NW Gully
SE Gully
A
B
C
D
Base of slump sheet
View looking SW up gully
f)
NE
SW
March 2014
Reference rock
A
B
Base of studied slump sheet
SE Gully
g)
SW
NE
March 2014
Modern fan gravels
NW Gully
Base of slump sheet
k)
NE
March 2014
Modern fan gravels
Top of case study slump
18 varves cycles
15 varves
Base of case study slump
Slumped beds
undeformed beds
Slumped beds
undeformed beds
h)
March 2015
A
B
C
a
B
NW Gully
SE Gully
View looking SW up gully
i)
NE
Reference rock
SW
March 2015
Top of case study slump
Base of case study slump
Slumped beds
Slumped beds
SE Gully
j)
March 2017
A
B
Base of slump sheet
Amount of new downcutting since March 2014
NW Gully
SE Gully
View looking SW up gully

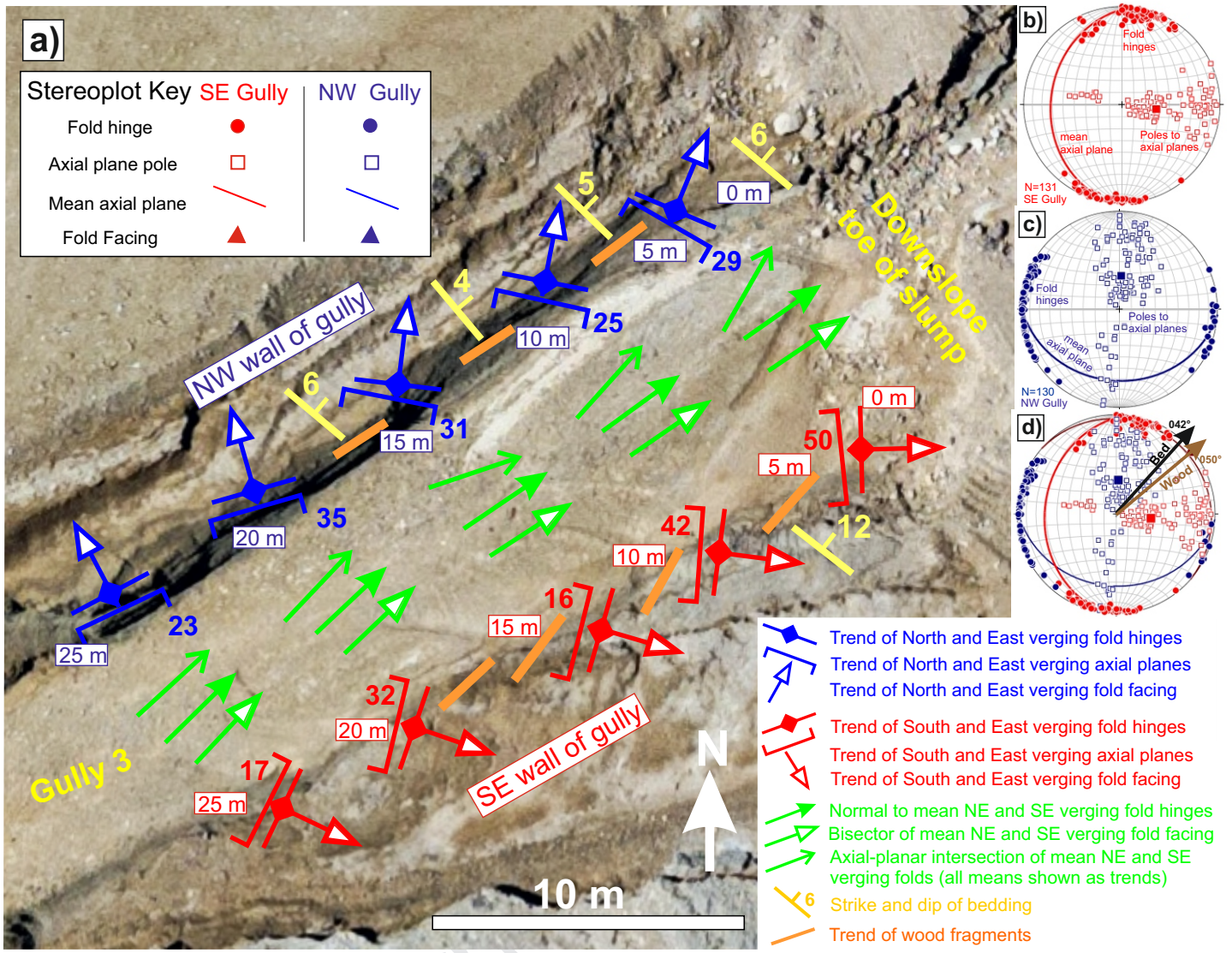
a)
Stereoplot Key
SE Gully
NW Gully
Fold hinge
Axial plane pole
Mean axial plane
Fold Facing
NW wall of gully
SE wall of gully
Gully 3
Downslope toe of slump
0 m
5 m
10 m
15 m
20 m
25 m
6
5
4
6
29
25
31
35
23
50
42
12
16
32
17
N
10 m
b)
Fold hinges
mean axial plane
Poles to axial planes
N=131
SE Gully
c)
Fold hinges
Poles to axial planes
mean axial plane
N=130
NW Gully
d)
042°
050°
Bed
Wood
Trend of North and East verging fold hinges
Trend of North and East verging axial planes
Trend of North and East verging fold facing
Trend of South and East verging fold hinges
Trend of South and East verging axial planes
Trend of South and East verging fold facing
Normal to mean NE and SE verging fold hinges
Bisector of mean NE and SE verging fold facing
Axial-planar intersection of mean NE and SE verging folds (all means shown as trends)
6
Strike and dip of bedding
Trend of wood fragments

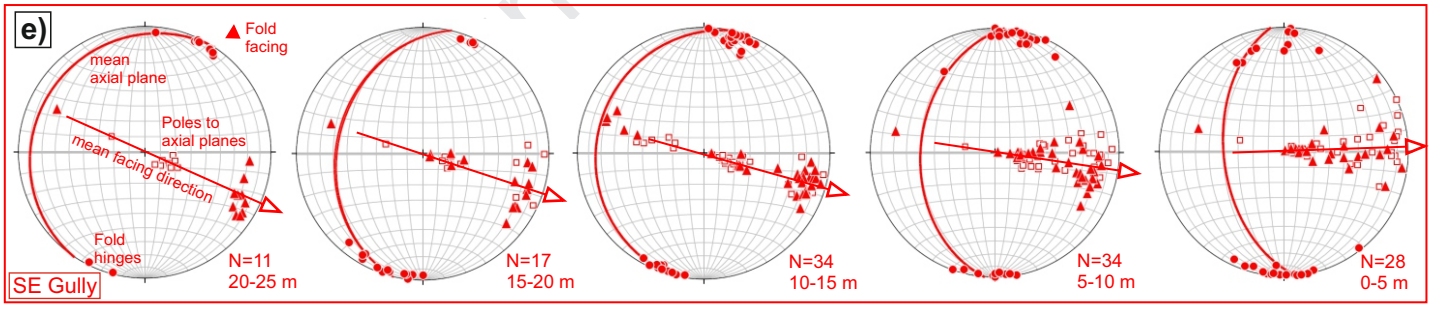
e)
Fold facing
mean axial plane
Poles to axial planes
mean facing direction
Fold hinges
SE Gully
N=11
20-25 m
N=17
15-20 m
N=34
10-15 m
N=34
5-10 m
N=28
0-5 m

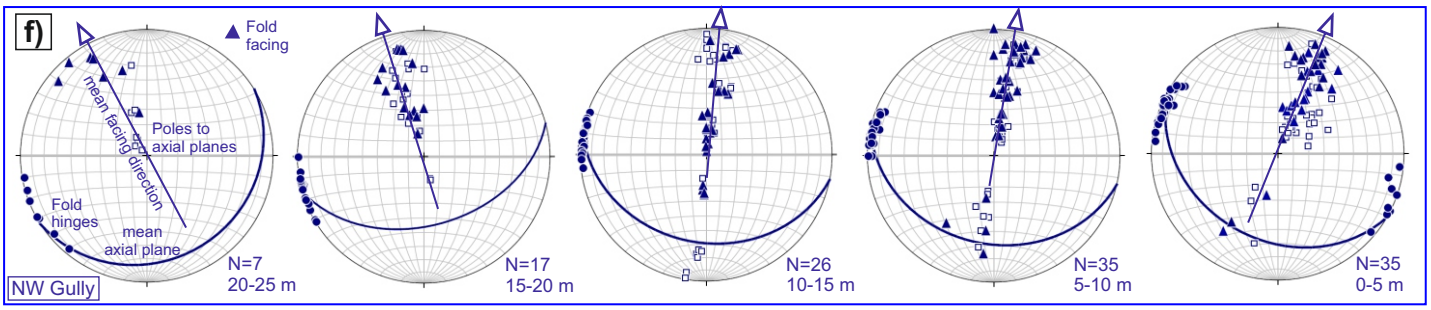
f)
Fold facing
mean facing direction
Poles to axial planes
Fold hinges
mean axial plane
NW Gully
N=7
20-25 m
N=17
15-20 m
N=26
10-15 m
N=35
5-10 m
N=35
0-5 m

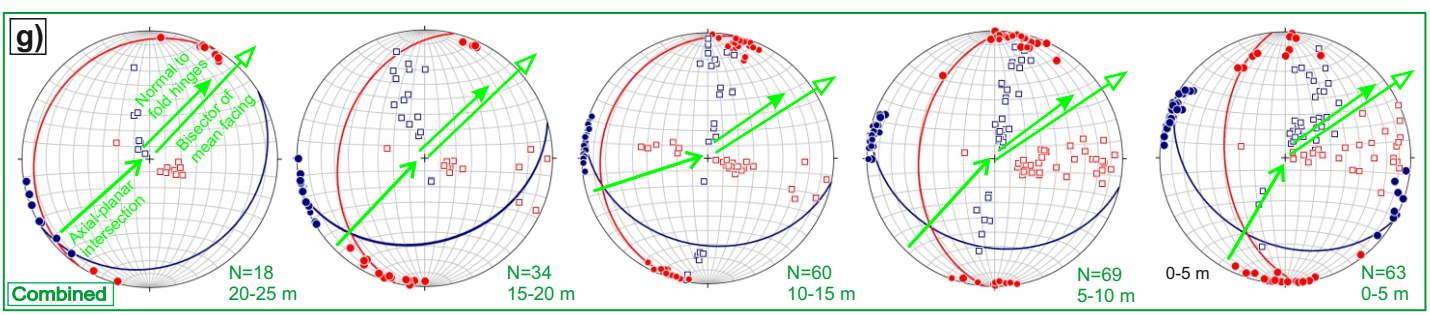
g)
Normal to fold hinges
Bisector of mean facing
Axial-planar intersection
Combined
N=18
20-25 m
N=34
15-20 m
N=60
10-15 m
N=69
5-10 m
0-5 m
N=63
0-5 m

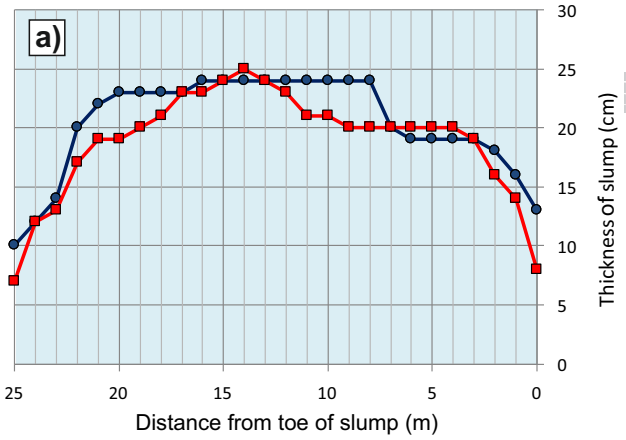
a)
Thickness of slump (cm)
Distance from toe of slump (m)

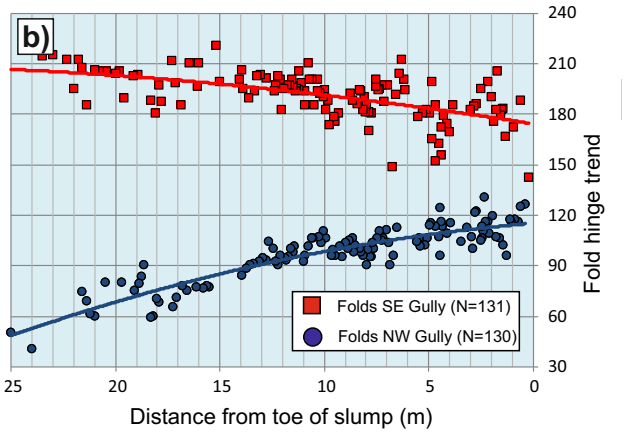
b)
Fold hinge trend
Folds SE Gully (N=131)
Folds NW Gully (N=130)
Distance from toe of slump (m)

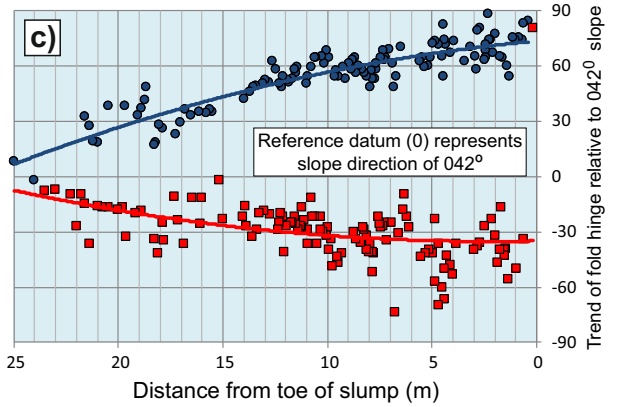
c)
Reference datum (0) represents slope direction of 042°
Trend of fold hinge relative to 042° slope
Distance from toe of slump (m)

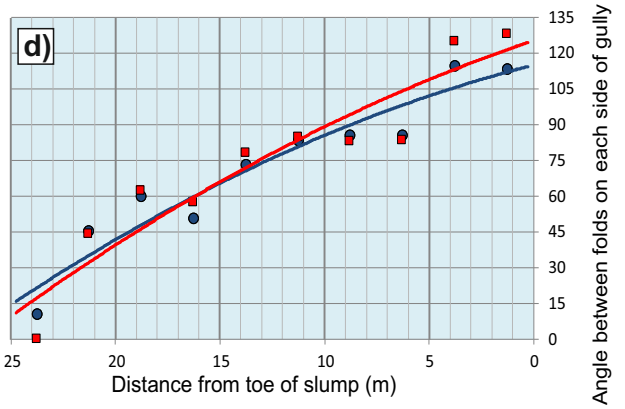
d)
Angle between folds on each side of gully
Distance from toe of slump (m)

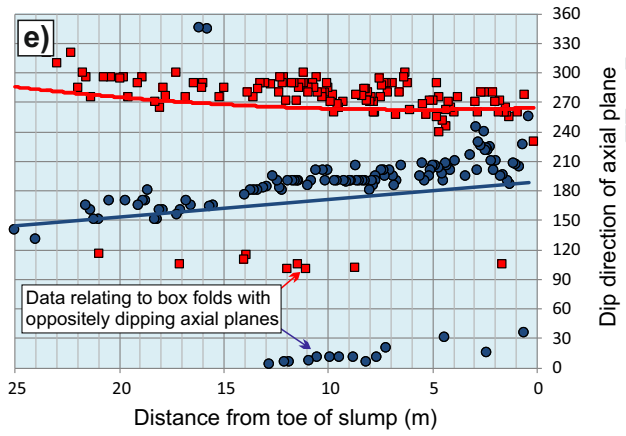
e)
Data relating to box folds with oppositely dipping axial planes
Dip direction of axial plane
Distance from toe of slump (m)

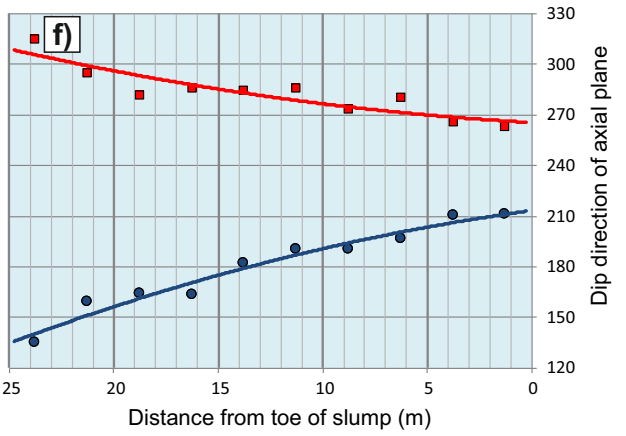
f)
Dip direction of axial plane
Distance from toe of slump (m)

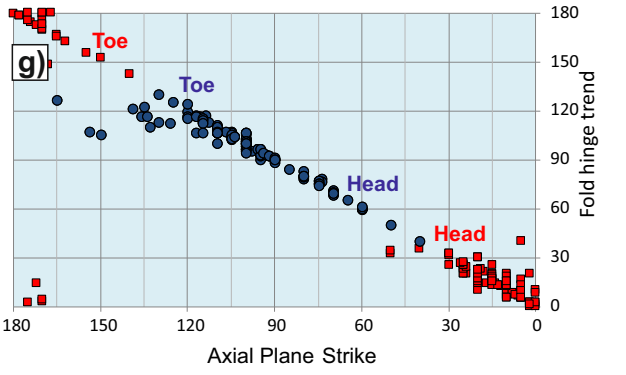
g)
Toe
Toe
Head
Head
Fold hinge trend
Axial Plane Strike

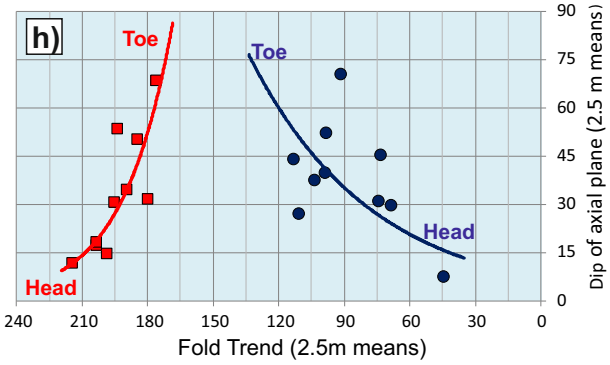
h)
Toe
Toe
Head
Head
Dip of axial plane (2.5 m means)
Fold Trend (2.5m means)

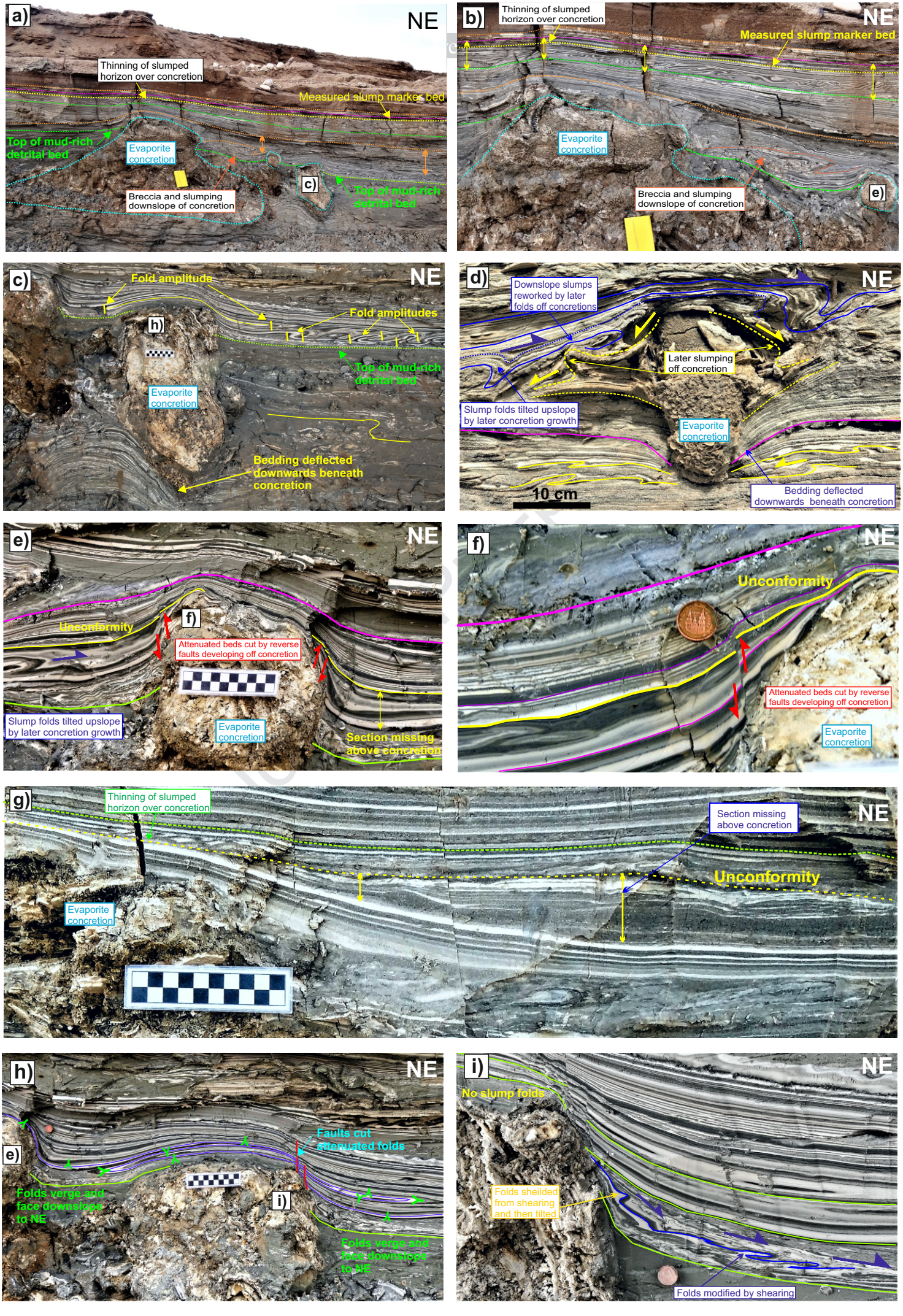
a)
NE
Thinning of slumped horizon over concretion
Measured slump marker bed
Top of mud-rich detrital bed
Evaporite concretion
Breccia and slumping downslope of concretion
c)
Top of mud-rich detrital bed
b)
Thinning of slumped horizon over concretion
NE
Measured slump marker bed
Evaporite concretion
Breccia and slumping downslope of concretion
e)
c)
NE
Fold amplitude
h)
Fold amplitudes
Top of mud-rich detrital bed
Evaporite concretion
Bedding deflected downwards beneath concretion
d)
NE
Downslope slumps reworked by later folds off concretions
Later slumping off concretion
Slump folds tilted upslope by later concretion growth
Evaporite concretion
10 cm
Bedding deflected downwards beneath concretion
e)
NE
Unconformity
f)
Attenuated beds cut by reverse faults developing off concretion
Slump folds tilted upslope by later concretion growth
Evaporite concretion
Section missing above concretion
f)
NE
Unconformity
Attenuated beds cut by reverse faults developing off concretion
Evaporite concretion
g)
Thinning of slumped horizon over concretion
Section missing above concretion
NE
Unconformity
Evaporite concretion
h)
NE
e)
Faults cut attenuated folds
Folds verge and face downslope to NE
i)
Folds verge and face downslope to NE
i)
NE
No slump folds
Folds sheilded from shearing and then tilted
Folds modified by shearing

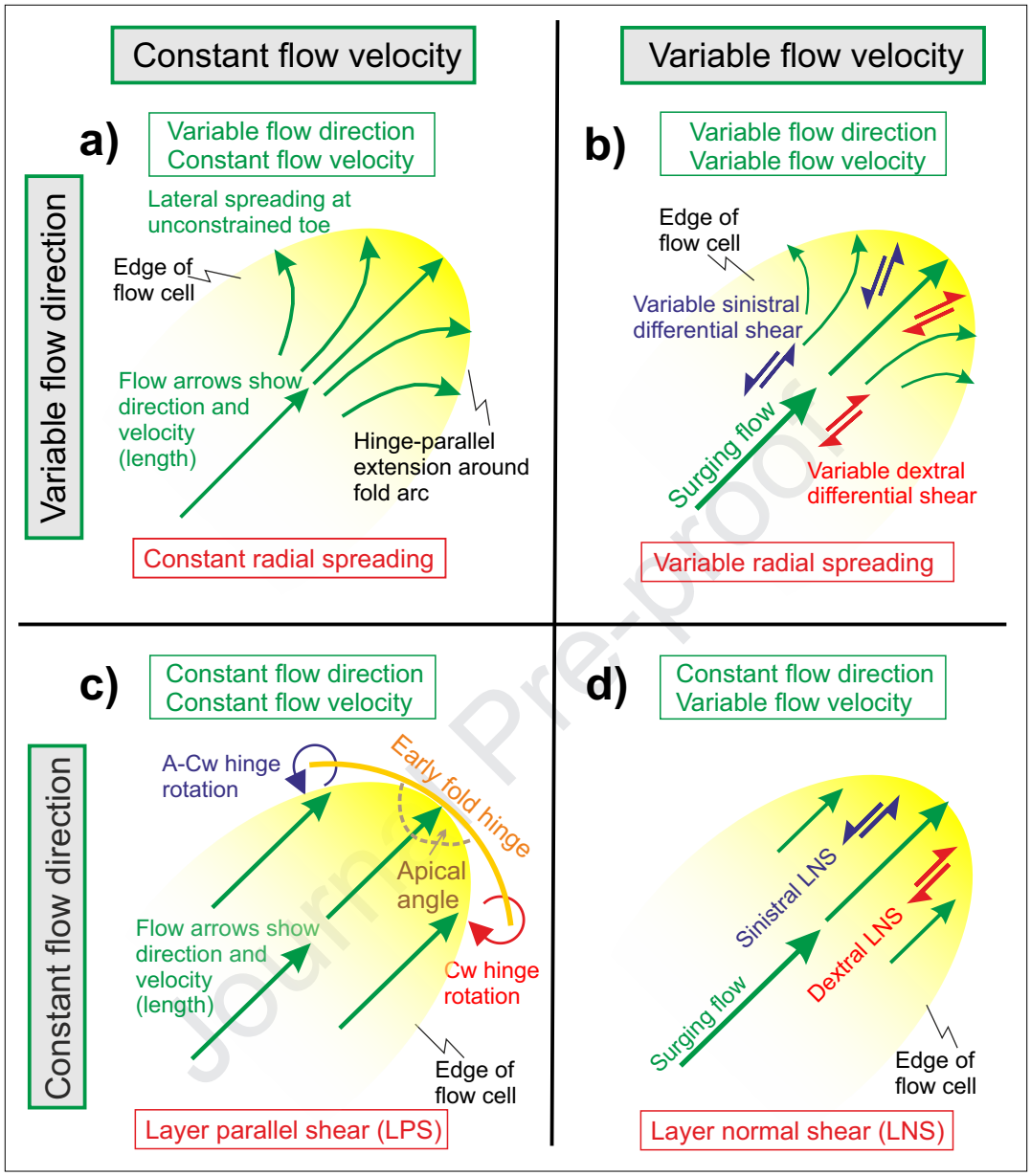

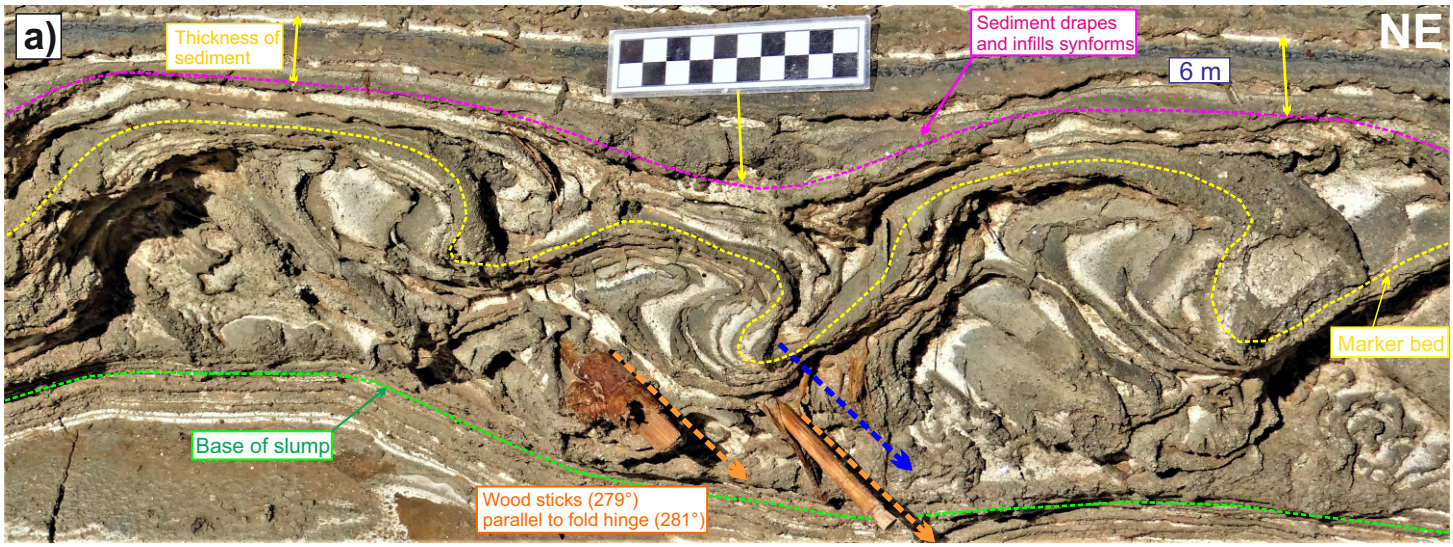
a)
Thickness of sediment
Sediment drapes and infills synforms
NE
6 m
Marker bed
Base of slump
Wood sticks (279°) parallel to fold hinge (281°)

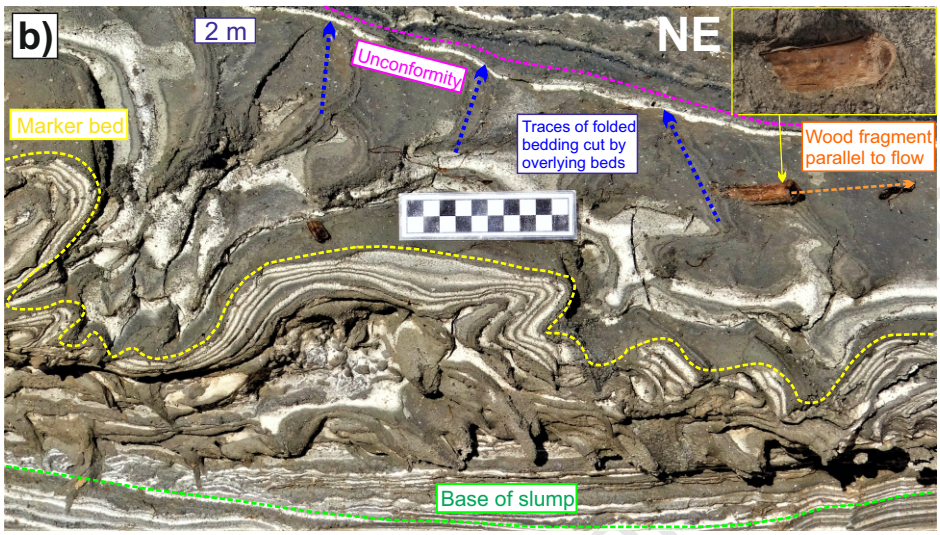
b)
2 m
NE
Unconformity
Marker bed
Traces of folded bedding cut by overlying beds
Wood fragment parallel to flow
Base of slump

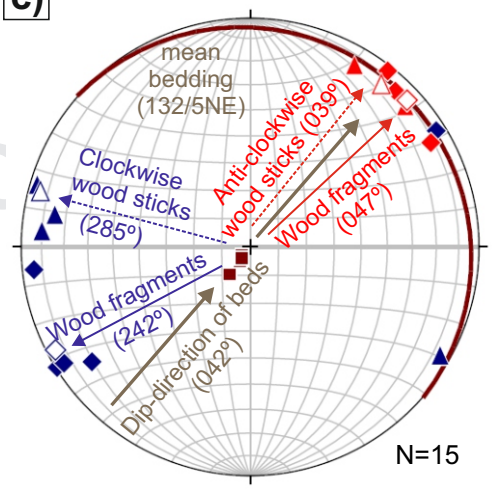
c)
mean bedding (132/5NE)
Clockwise wood sticks (285°)
Anti-clockwise wood sticks (039°)
Wood fragments (047°)
Wood fragments (242°)
Dip-direction of beds (042°)
N=15

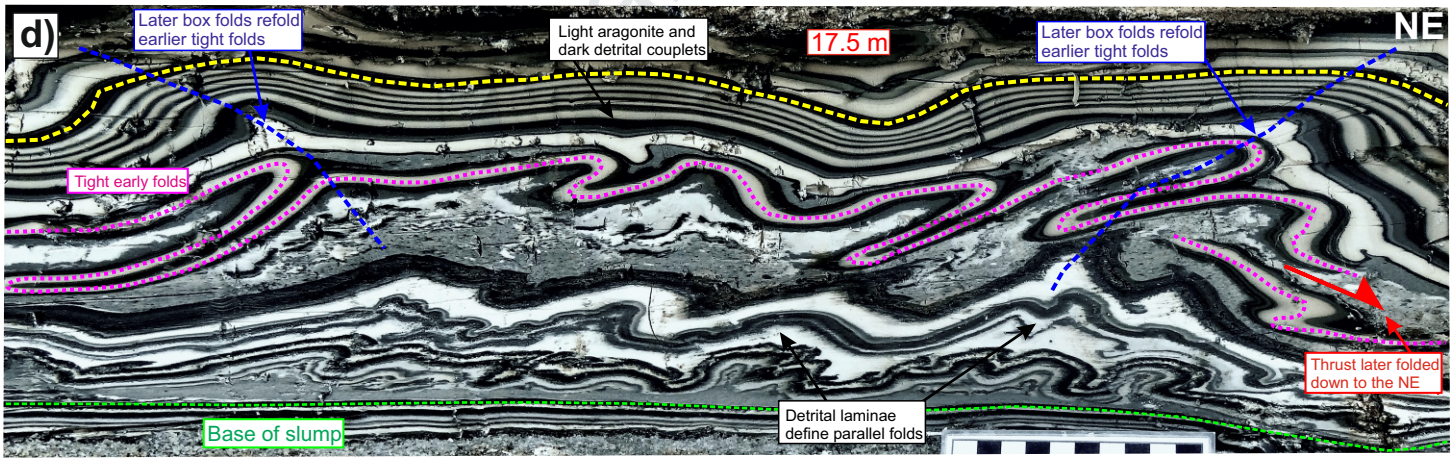
d)
Later box folds refold earlier tight folds
Light aragonite and dark detrital couplets
17.5 m
Later box folds refold earlier tight folds
NE
Tight early folds
Thrust later folded down to the NE
Detrital laminae define parallel folds
Base of slump

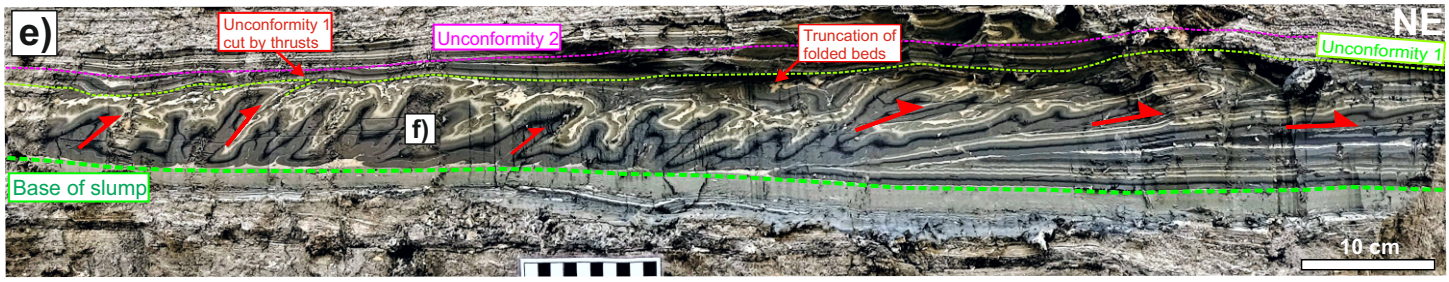
e)
Unconformity 1 cut by thrusts
Unconformity 2
Truncation of folded beds
NE
Unconformity 1
f)
Base of slump
10 cm

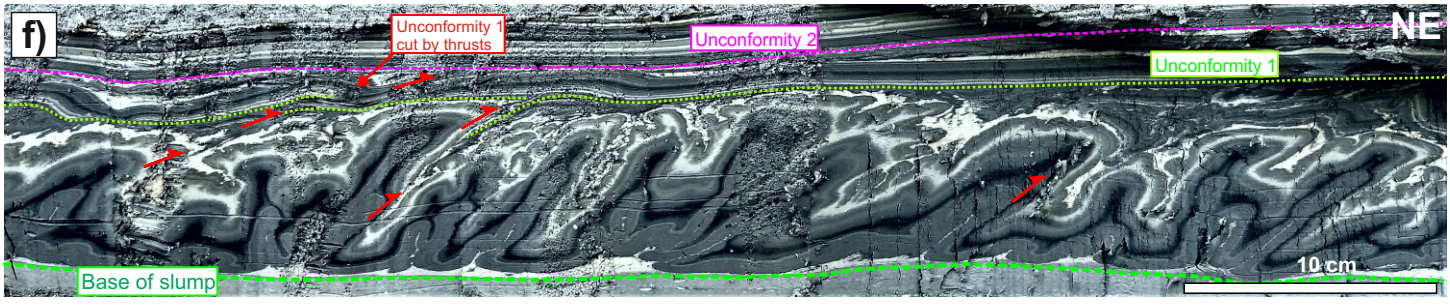
f)
Unconformity 1 cut by thrusts
Unconformity 2
NE
Unconformity 1
Base of slump
10 cm

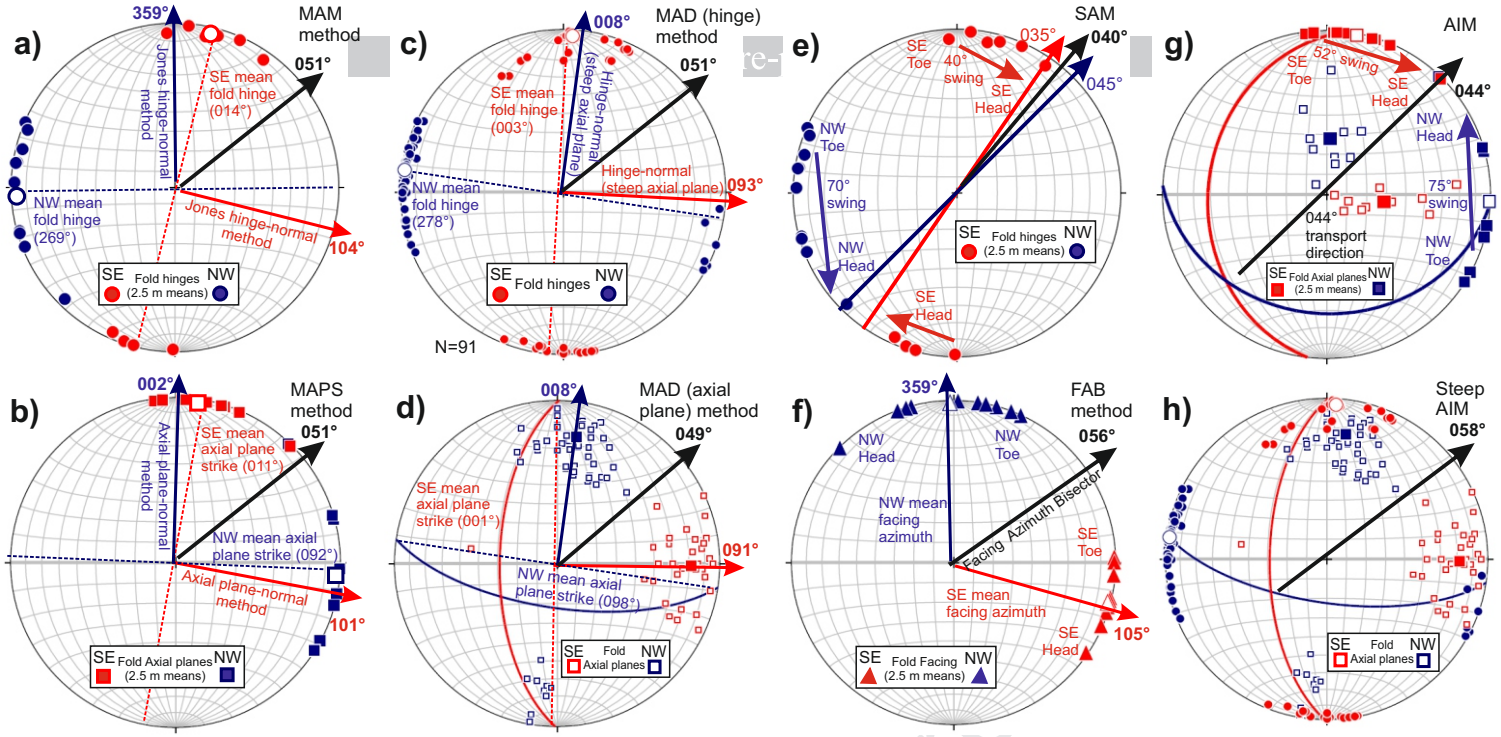

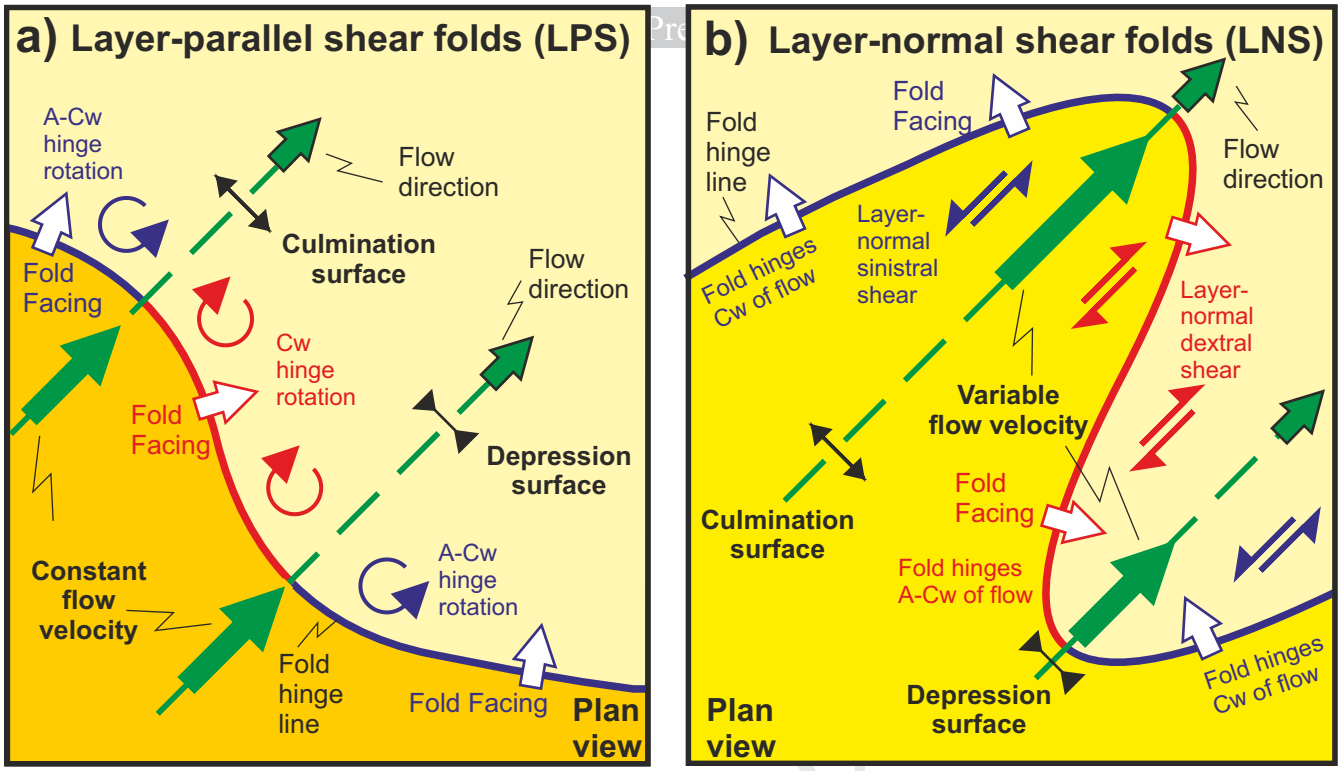

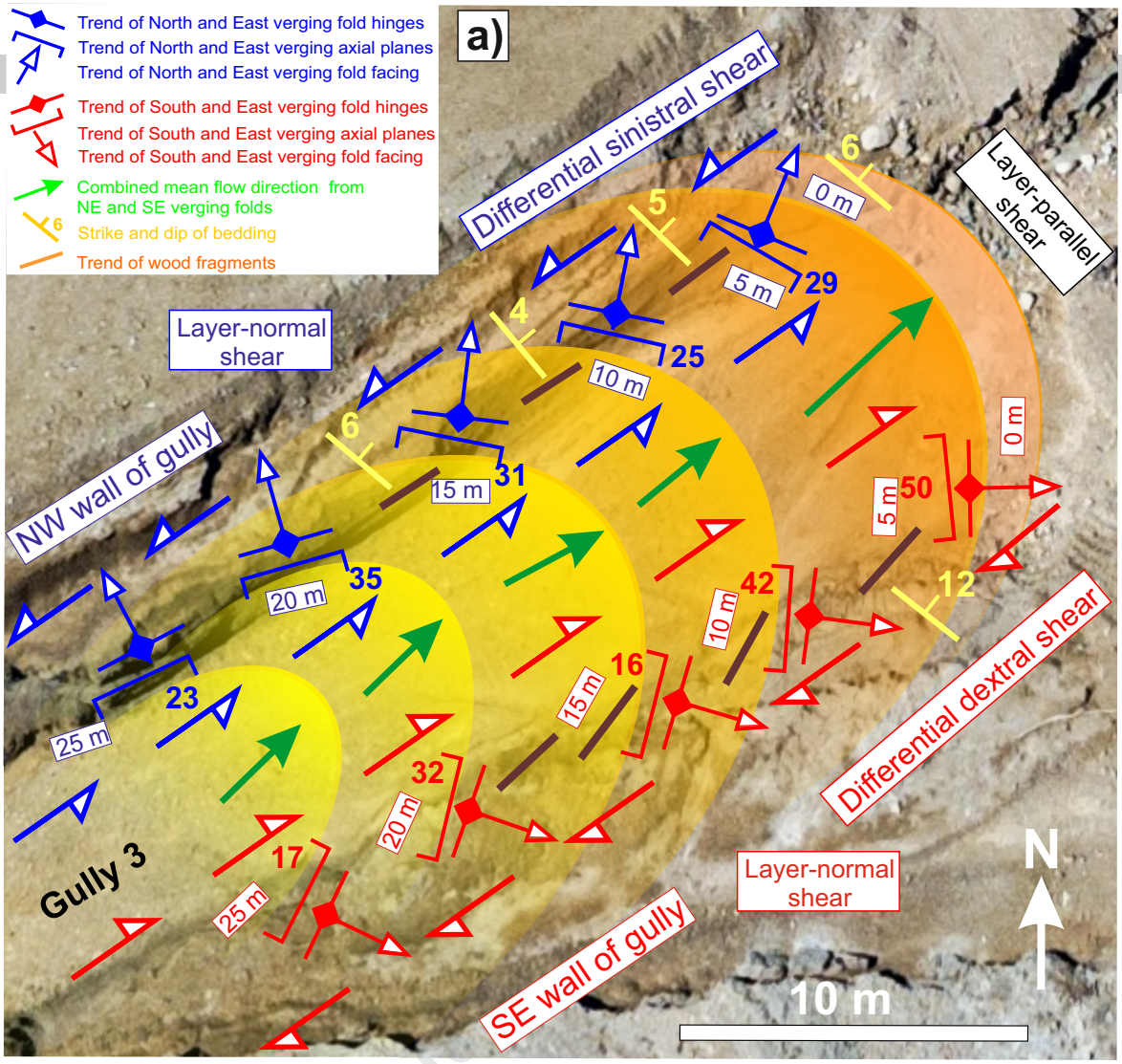
a)
Trend of North and East verging fold hinges
Trend of North and East verging axial planes
Trend of North and East verging fold facing
Trend of South and East verging fold hinges
Trend of South and East verging axial planes
Trend of South and East verging fold facing
Combined mean flow direction from NE and SE verging folds
Strike and dip of bedding
Trend of wood fragments
Differential sinistral shear
Layer-parallel shear
Layer-normal shear
NW wall of gully
Differential dextral shear
Layer-normal shear
SE wall of gully
Gully 3
N
10 m
0 m
5 m
10 m
15 m
20 m
25 m
29
25
31
35
23
32
17
16
42
50
12
6
5
4

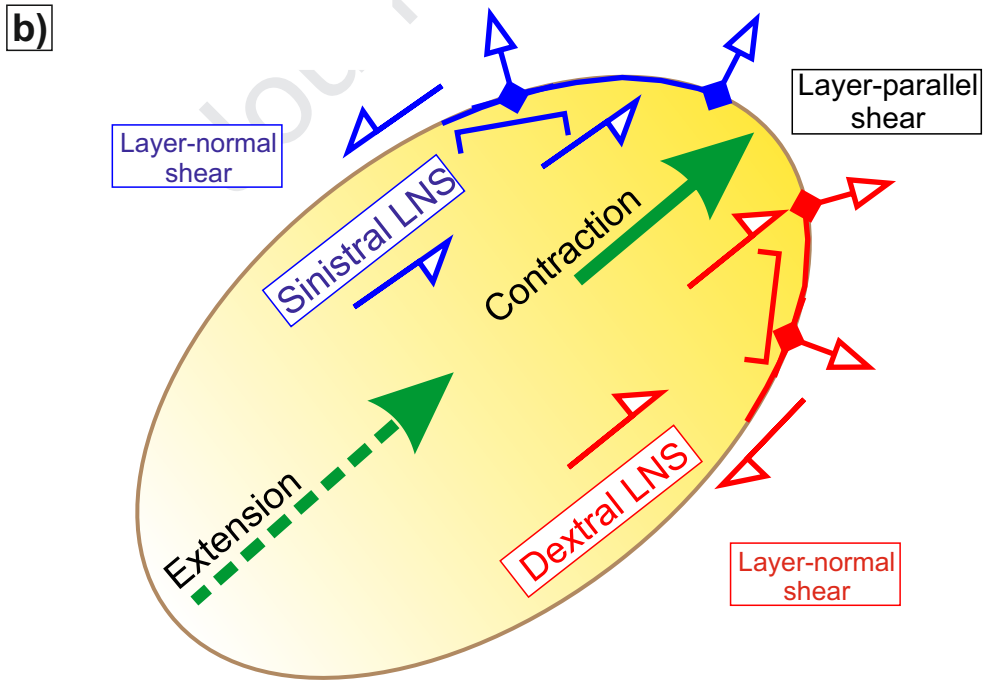
b)
Layer-normal shear
Layer-parallel shear
Sinistral LNS
Contraction
Extension
Dextral LNS
Layer-normal shear

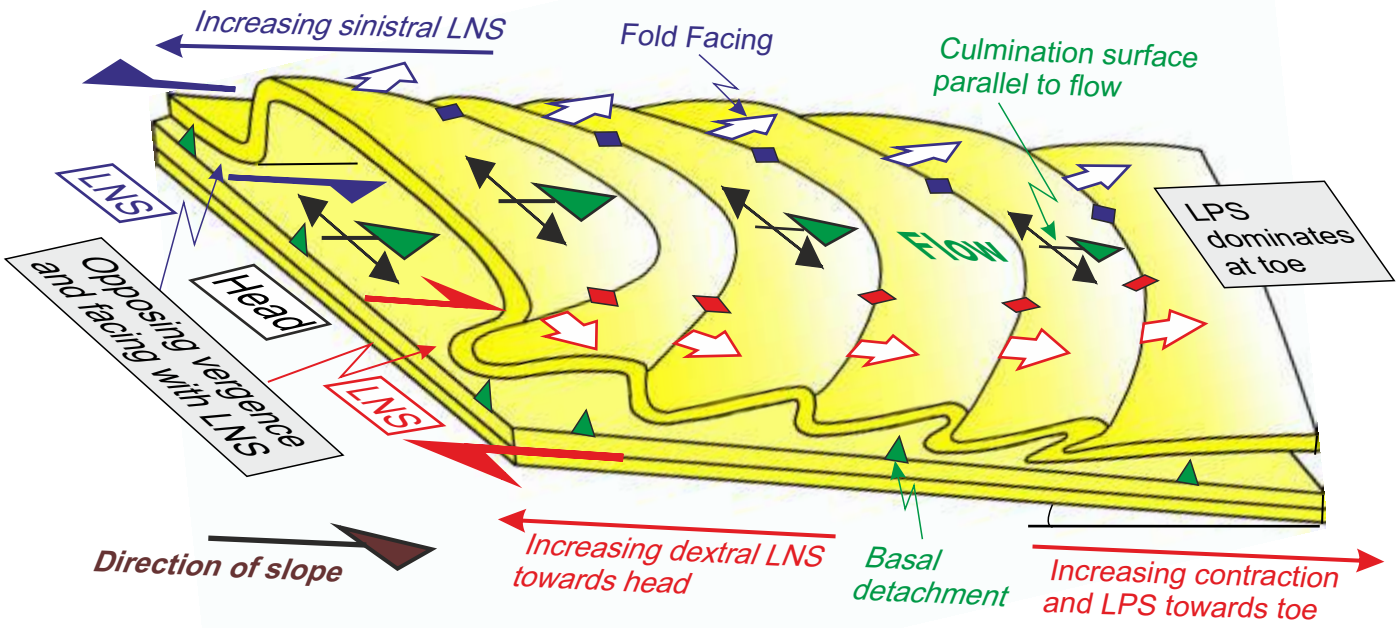

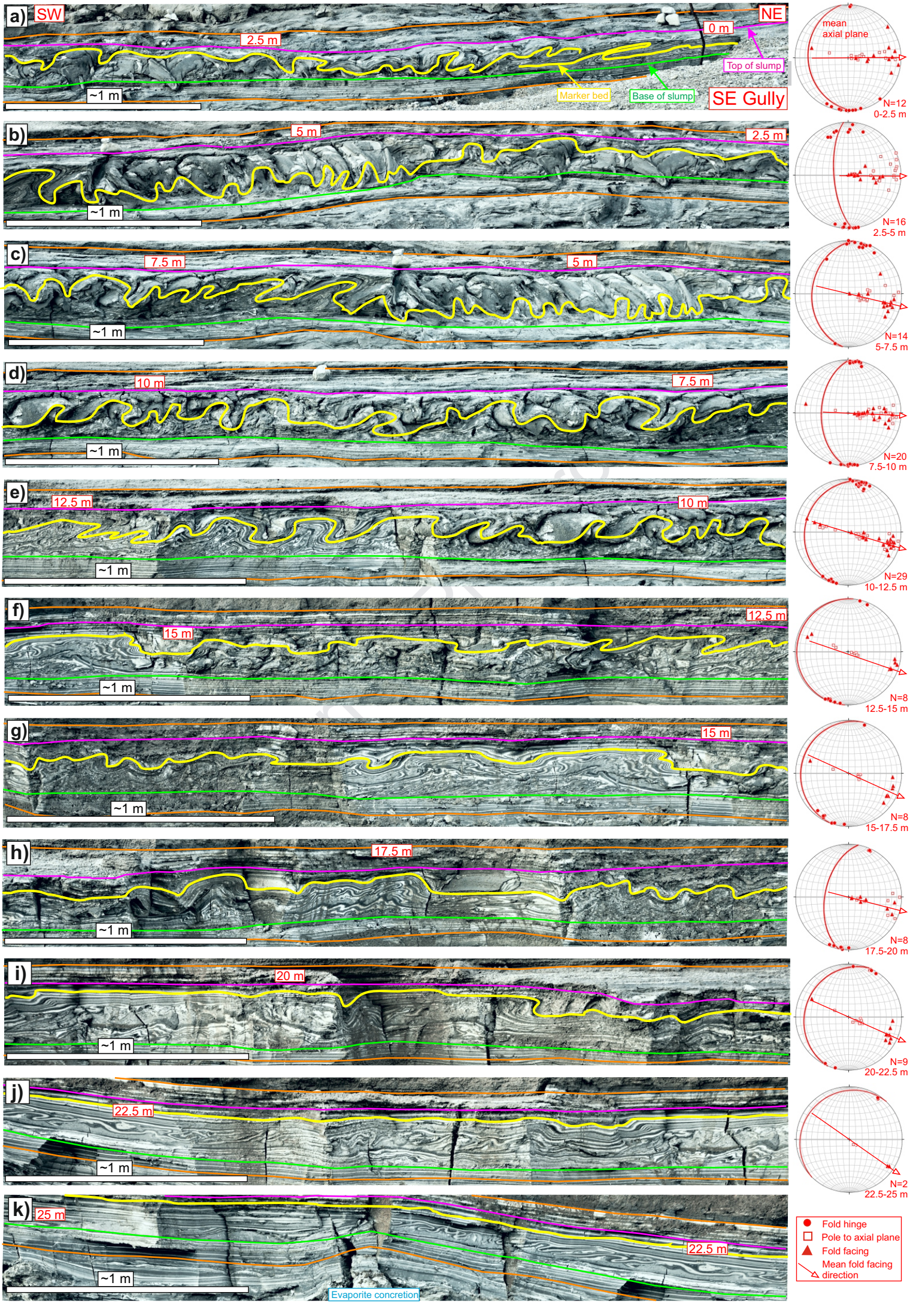
a)
SW
NE
2.5 m
0 m
Top of slump
Marker bed
Base of slump
SE Gully
~1 m
mean
axial plane
N=12
0-2.5 m
b)
5 m
2.5 m
~1 m
N=16
2.5-5 m
c)
7.5 m
5 m
~1 m
N=14
5-7.5 m
d)
10 m
7.5 m
~1 m
N=20
7.5-10 m
e)
12.5 m
10 m
~1 m
N=29
10-12.5 m
f)
15 m
12.5 m
~1 m
N=8
12.5-15 m
g)
15 m
~1 m
N=8
15-17.5 m
h)
17.5 m
~1 m
N=8
17.5-20 m
i)
20 m
~1 m
N=9
20-22.5 m
j)
22.5 m
~1 m
N=2
22.5-25 m
k)
25 m
22.5 m
~1 m
Evaporite concretion
Fold hinge
Pole to axial plane
Fold facing
Mean fold facing direction

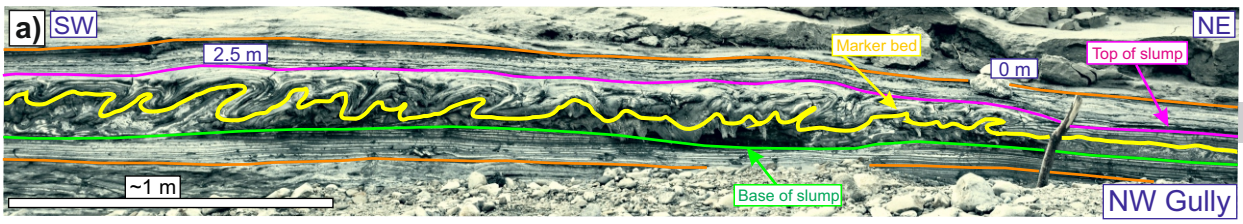
a)
SW
NE
2.5 m
Marker bed
0 m
Top of slump
~1 m
Base of slump
NW Gully

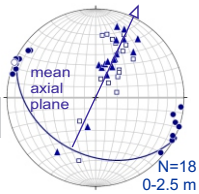
mean
axial
plane
N=18
0-2.5 m

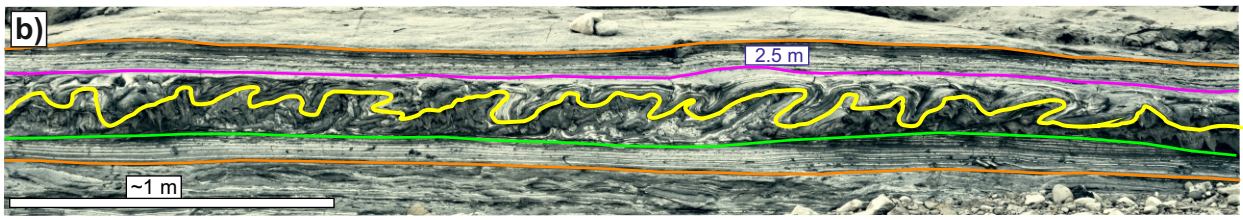
b)
2.5 m
~1 m

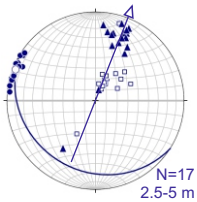
N=17
2.5-5 m

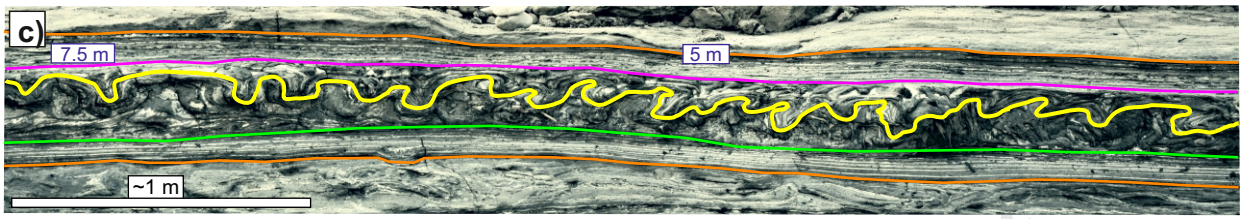
c)
7.5 m
5 m
~1 m

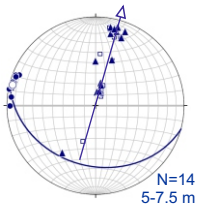
N=14
5-7.5 m

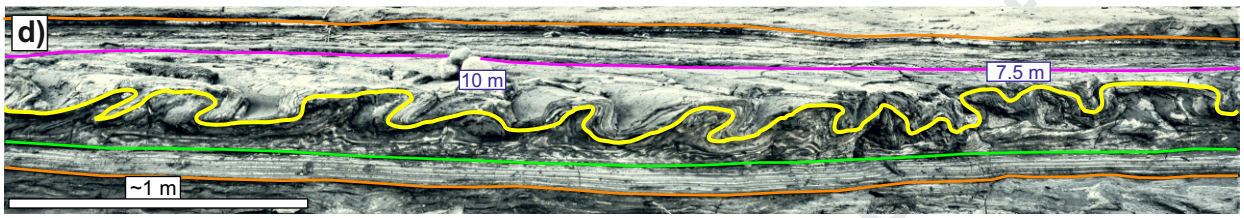
d)
10 m
7.5 m
~1 m

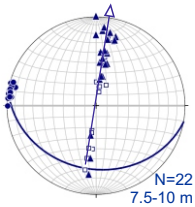
N=22
7.5-10 m

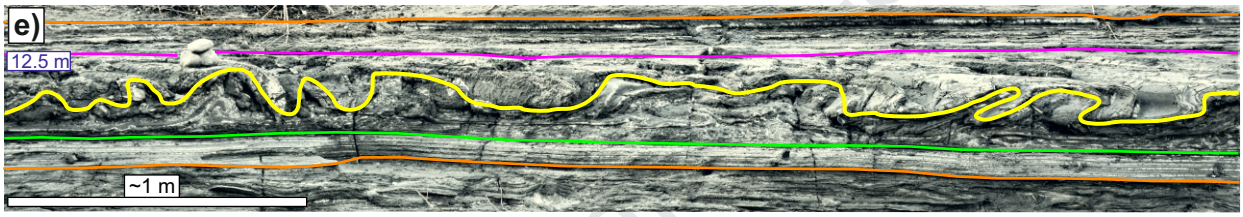
e)
12.5 m
~1 m

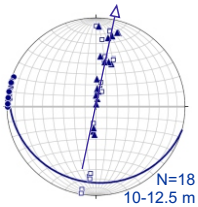
N=18
10-12.5 m

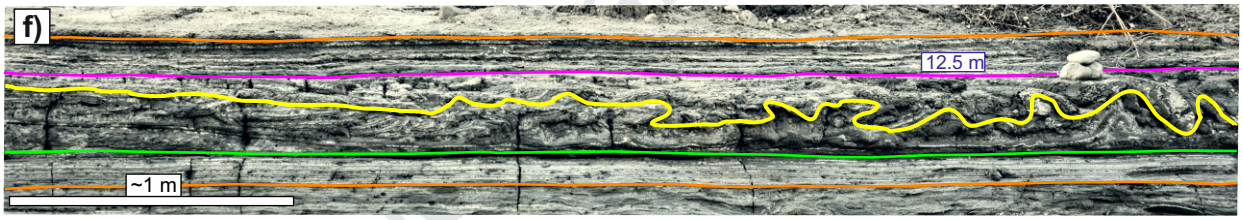
f)
12.5 m
~1 m

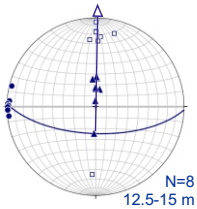
N=8
12.5-15 m

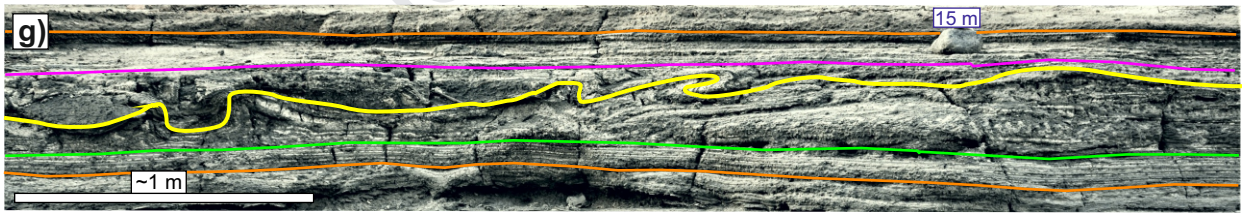
g)
15 m
~1 m

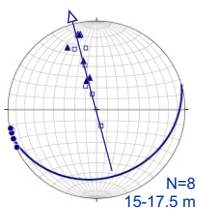
N=8
15-17.5 m

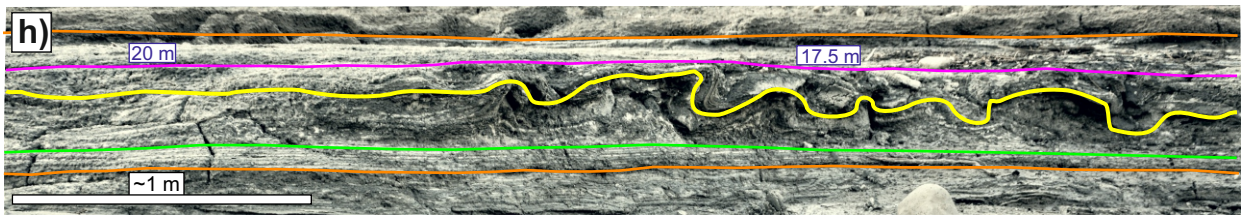
h)
20 m
17.5 m
~1 m

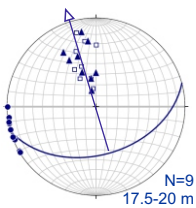
N=9
17.5-20 m

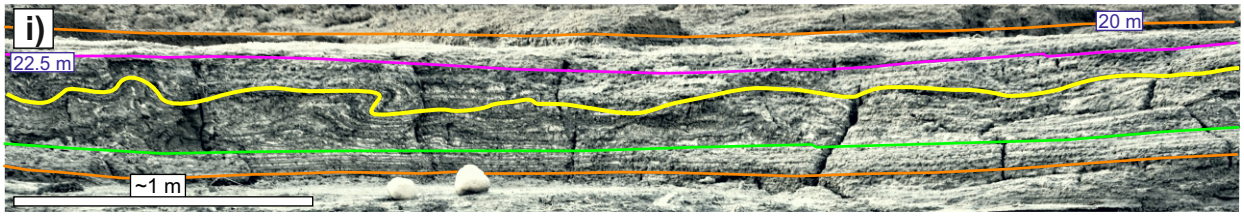
i)
20 m
22.5 m
~1 m

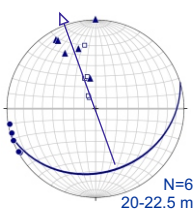
N=6
20-22.5 m

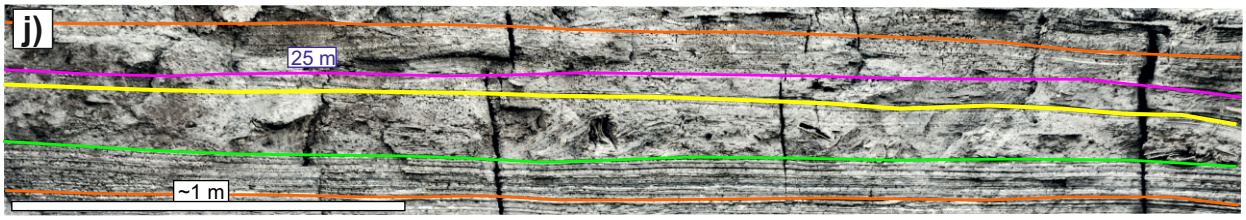
j)
25 m
~1 m

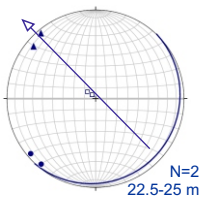
N=2
22.5-25 m

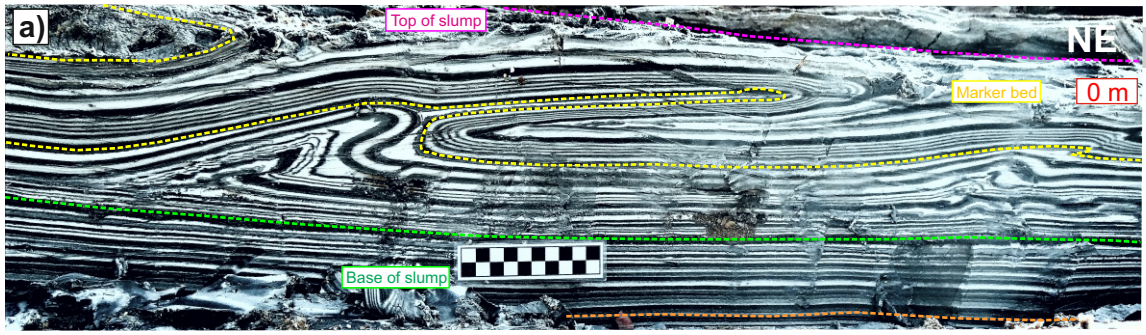
a)
Top of slump
NE
Marker bed
0 m
Base of slump

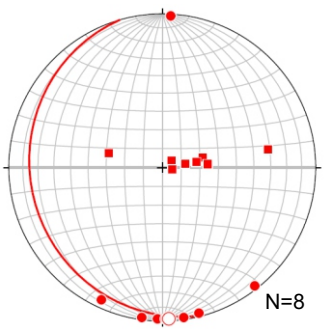
N=8

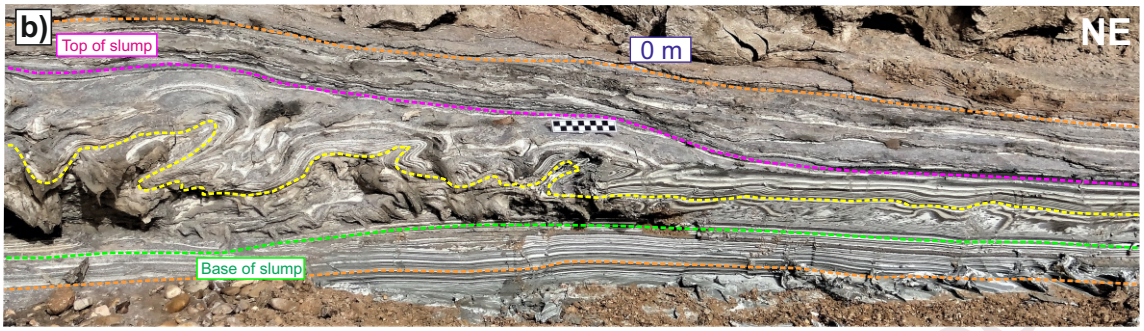
b)
Top of slump
0 m
NE
Base of slump

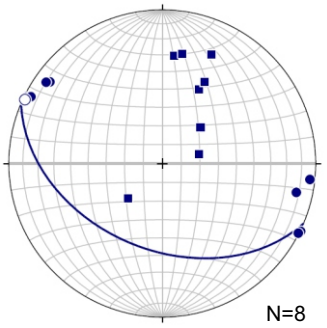
N=8

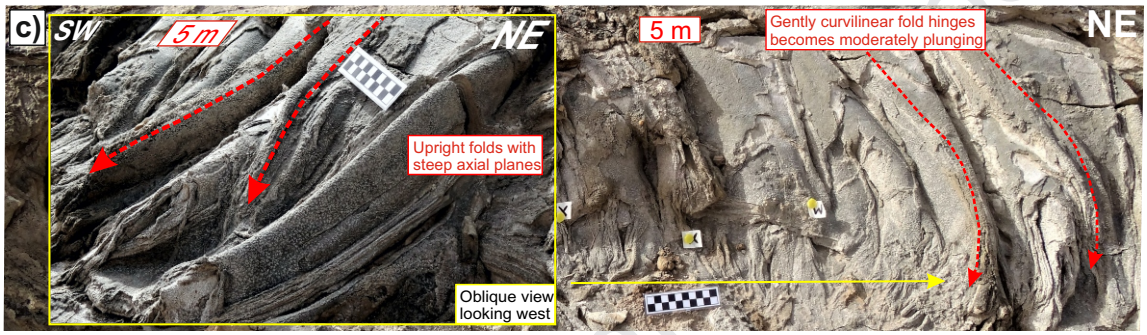
c)
SW
5 m
NE
Upright folds with steep axial planes
Oblique view looking west
5 m
Gently curvilinear fold hinges becomes moderately plunging
NE

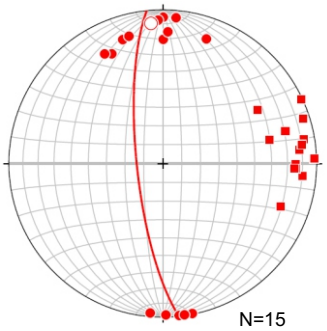
N=15

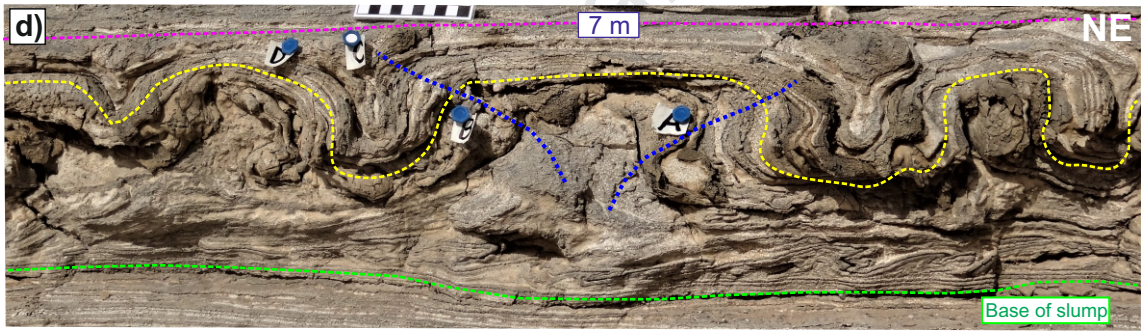
d)
7 m
NE
Base of slump

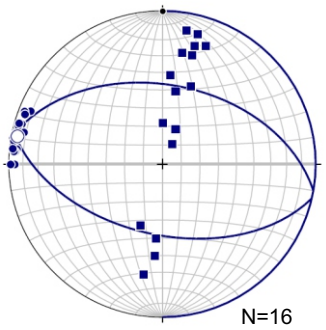
N=16

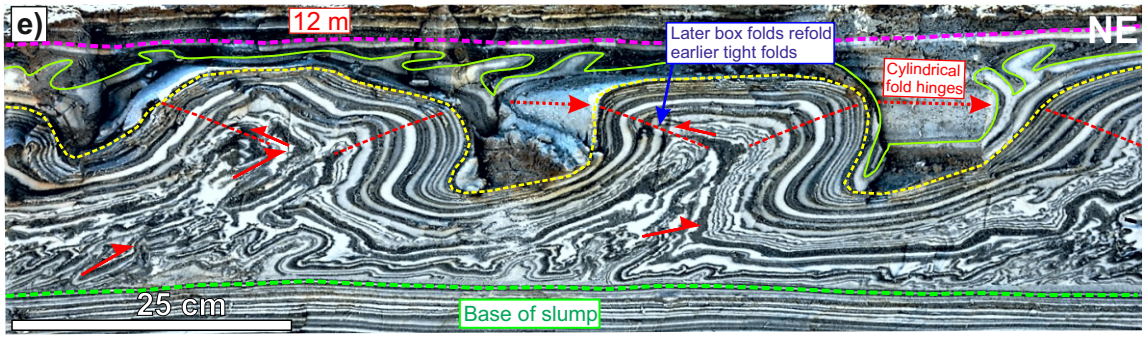
e)
12 m
Later box folds refold earlier tight folds
Cylindrical fold hinges
NE
25 cm
Base of slump

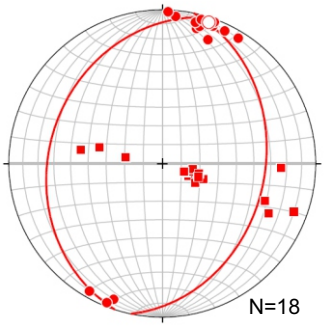
N=18

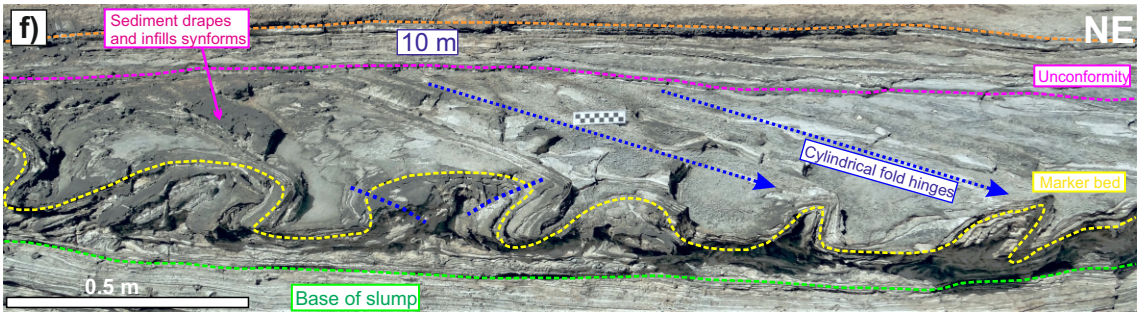
f)
Sediment drapes and infills synforms
10 m
NE
Unconformity
Cylindrical fold hinges
Marker bed
0.5 m
Base of slump

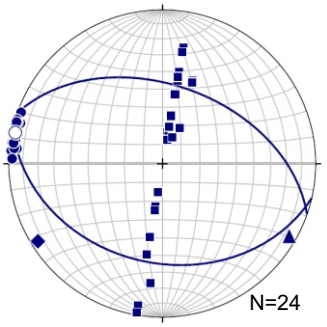
N=24

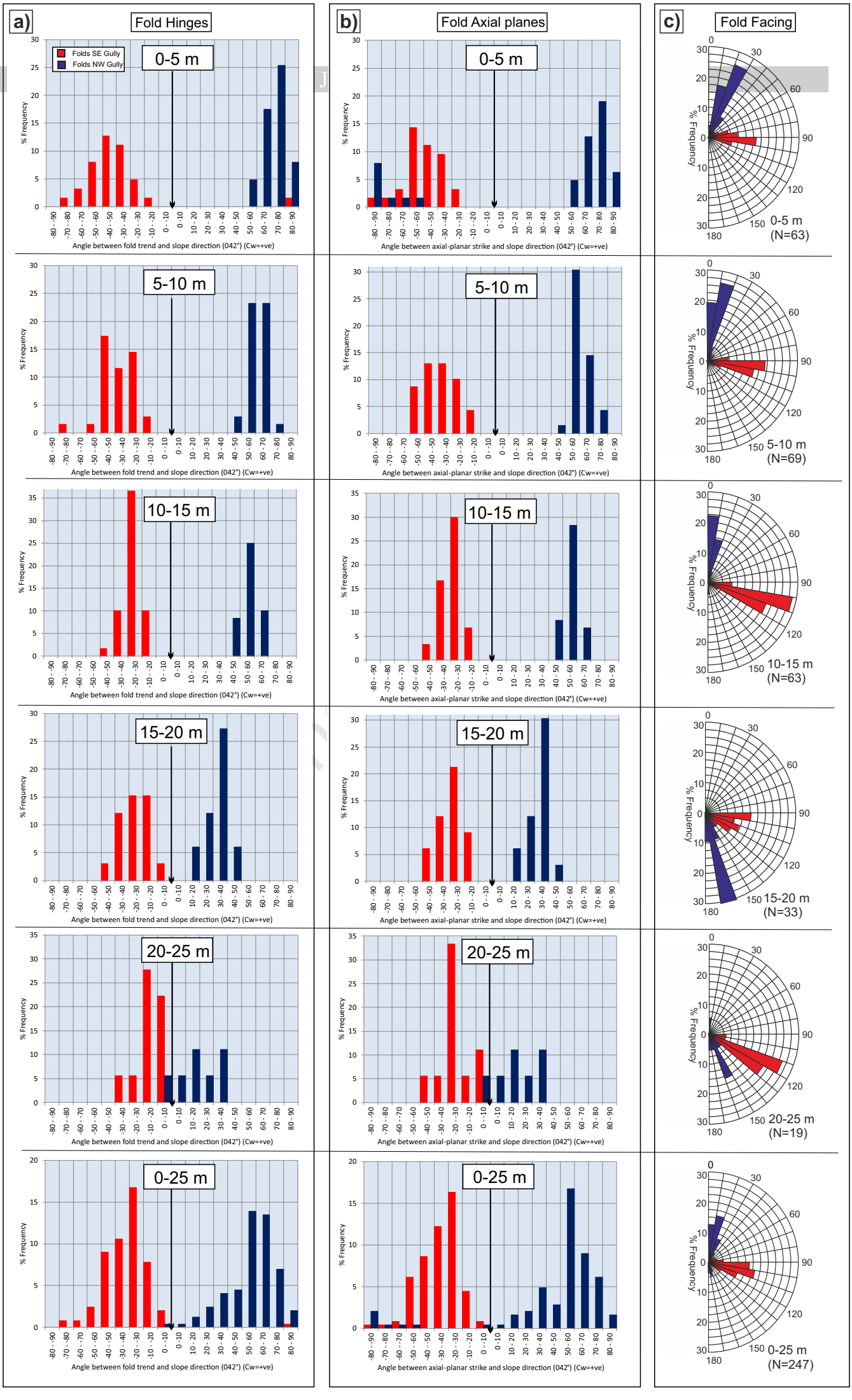
a)
Fold Hinges
b)
Fold Axial planes
c)
Fold Facing
Folds SE Gully
Folds NW Gully
0-5 m
5-10 m
10-15 m
15-20 m
20-25 m
0-25 m
% Frequency
Angle between fold trend and slope direction (042°) (Cw=+ve)
Angle between axial-planar strike and slope direction (042°) (Cw=+ve)
0-5 m (N=63)
5-10 m (N=69)
10-15 m (N=63)
15-20 m (N=33)
20-25 m (N=19)
0-25 m (N=247)

Highlights

Recent falls in the Dead Sea water level have exposed a modern unconsolidated mass transport deposit (MTD) preserved in wet sediments.

Recurrent failure of a relatively steep (5°-10°) slope suggests downslope creep of the MTD.

Four general models potentially explain variable fold hinge and axial plane orientations around ‘flow lobes’ within MTDs.

Evaluation of complete fold data sets leads to slope estimates within 10° of the observed slope, whereas partial data sets suggest ‘palaeoslope’ orientations that are inaccurate by up to 90°.

Variable flow creates a range of structures at different times and in different parts of an MTD. Incomplete data may provide incorrect estimates of palaeoslope orientations in the ancient rock record.

We can confirm that there are no conflicts of interest with this work.